



High-redshift Galaxy Formation with Self-consistently Modeled Stars and Massive Black Holes: Stellar Feedback and Quasar Growth

Ji-hoon Kim¹ , John H. Wise² , Tom Abel^{3,4}, Yongseok Jo¹, Joel R. Primack⁵ , and Philip F. Hopkins⁶ ¹ Center for Theoretical Physics, Department of Physics and Astronomy, Seoul National University, Seoul 08826, Republic of Korea; me@jihoonkim.org² Center for Relativistic Astrophysics, School of Physics, Georgia Institute of Technology, Atlanta, GA 30332, USA³ Kavli Institute for Particle Astrophysics and Cosmology, SLAC National Accelerator Laboratory, Menlo Park, CA 94025, USA⁴ Department of Physics, Stanford University, Stanford, CA 94305, USA⁵ Department of Physics, University of California at Santa Cruz, Santa Cruz, CA 95064, USA⁶ TAPIR, Department of Astronomy, California Institute of Technology, Pasadena, CA 91125, USA

Received 2019 August 9; revised 2019 October 21; accepted 2019 October 23; published 2019 December 16

Abstract

As computational resolution of modern cosmological simulations come closer to resolving individual star-forming clumps in a galaxy, the need for “resolution-appropriate” physics for a galaxy-scale simulation has never been greater. To this end, we introduce a self-consistent numerical framework that includes explicit treatments of feedback from star-forming molecular clouds (SFMCs) and massive black holes (MBHs). In addition to the thermal supernovae feedback from SFMC particles, photoionizing radiation from both SFMCs and MBHs is tracked through full three-dimensional ray tracing. A mechanical feedback channel from MBHs is also considered. Using our framework, we perform a state-of-the-art cosmological simulation of a quasar-host galaxy at $z \sim 7.5$ for ~ 25 Myr with all relevant galactic components, such as dark matter, gas, SFMCs, and an embedded MBH seed of $\gtrsim 10^6 M_\odot$. We find that feedback from SFMCs and an accreting MBH suppresses runaway star formation locally in the galactic core region. Newly included radiation feedback from SFMCs, combined with feedback from the MBH, helps the MBH grow faster by retaining gas that eventually accretes on to the MBH. Our experiment demonstrates that previously undiscussed types of interplay between gas, SFMCs, and a MBH may hold important clues about the growth and feedback of quasars and their host galaxies in the high-redshift universe.

Unified Astronomy Thesaurus concepts: Galaxy dynamics (591); Galaxy evolution (594); Galaxy kinematics (602); Galaxy formation (595); Galaxy nuclei (609); Star formation (1569); Galaxy circumnuclear disk (581); Active galactic nuclei (16); Quasars (1319); Supermassive black holes (1663); Interstellar medium (847)

1. Introduction

The very massive black holes (MBHs) lurking at the centers of many large galaxies in the universe have been the topic of hard-working observers and theorists over the past decades. The consensus view is that these MBHs and their host galaxies have grown together under each other’s influence. Moreover, observations indicate that extremely MBHs of mass $\gtrsim 10^9 M_\odot$ started to exist in the $z > 7$ era, only a few hundred Myr after the big bang (e.g., Mortlock et al. 2011; Bañados et al. 2018), and many more prevailed in the $z \sim 6$ era (e.g., Venemans et al. 2013; Wu et al. 2015). The discovery of surprisingly MBHs in the early universe inevitably raises intriguing questions about our understanding of the universe: how did MBHs acquire such large masses in such a short time? Do we need any new physical mechanism to explain the rapid growth of MBHs? How do MBHs interact with the interstellar medium (ISM) of their host galaxies? Do high- z MBHs imply that the age of the universe estimated by the standard Λ CDM cosmology is inaccurate after all? Therefore, the evolution of MBHs in the early universe is considered to be an ultimate testing ground for our contemporary understandings of astrophysics, black hole physics, and cosmology.

A commonly referred scenario for a high- z MBH formation begins with a remnant black hole of tens of solar masses that forms when a first generation Population III star dies at $z \gtrsim 10$. A sequence of galaxy mergers and the subsequent merging of their embedded black holes are thought to have led to a $\gtrsim 10^9 M_\odot$ MBH by $z > 7$ (e.g., Haiman & Loeb 2001; Volonteri 2010, see also other scenarios with more massive seed black holes such as direct collapse black holes—to be discussed in Section 4.1). A

numerical evaluation of this hypothesis requires us to implement *self-consistent* physics models surrounding the evolution of MBHs in simulations: how is the interstellar gas consumed through star formation and MBH accretion? How do radiation and winds from the MBHs in turn self-regulate the growth of their own and their host galaxies? How do young stars’ radiation and supernovae explosions curb subsequent star formation and keep the interstellar gas from being hastily consumed? An unabridged, self-consistent modeling of how galactic ingredients—i.e., gas, stars, and MBHs—interact with one another at different scales is crucial to numerically probe the evolution of MBHs.

Aided by the advances in parallel computing, modern cosmological simulations with large computational domains (of at least $\gtrsim 10$ Mpc) are now starting to resolve structures as small as individual star-forming clouds (of $\lesssim 10$ pc) inside a galaxy (e.g., Ceverino et al. 2018; Hopkins et al. 2018; Kim et al. 2018). This type of high-resolution simulation is an ideal vehicle to investigate how a high- z MBH grew because we can now resolve gas inflows from large to small scales simultaneously, which allows us to sample one or more sufficiently massive MBH seeds. These simulations will be indispensable to fully grasp how the small-scale physics of MBHs is tightly linked with overall galactic evolution and morphology. However, note that even a simulation with the best numerical resolution would not be useful to its full potential unless it is accompanied by self-consistent physics models that are appropriate at that particular resolution. In fact, a high-resolution simulation without “resolution-appropriate” physics models could very well produce meaningless, if not inaccurate, results. For example, for a kpc-resolution simulation,

a simple stellar feedback prescription that describes only supernovae explosions is likely to be sufficient. But for a pc-resolution simulation with a corresponding timestep of $\Delta t \sim 3 \times 10^4$ yr at 10^4 K, a better feedback prescription is required that includes early channels, such as photoionizing radiation from young stars (ages of $\lesssim 3$ Myr $\simeq 100 \Delta t$; see e.g., Kim et al. 2013a; Stinson et al. 2013; Hopkins et al. 2018). Without a temporally resolved stellar feedback model that is appropriate for the resolution, even the pc-resolution simulation would not be useful to its full potential.

Despite the best recent efforts (e.g., Hopkins & Quataert 2010; Sijacki et al. 2015; DeGraf & Sijacki 2017; Weinberger et al. 2017; Hopkins et al. 2018; Trebitsch et al. 2018), the numerical galaxy-MBH formation community is yet to converge on “resolution-appropriate” physics models that are compatible with the best resolution in the field ($\lesssim 10$ pc). Instead, previous galaxy-MBH formation simulations have sometimes had recourse to empirically tuned sub-resolution recipes, such as boosted Bondi accretion estimates, or bimodal feedback channels—quasar- and radio-mode—for MBHs. While these prescriptions have been instrumental in calculations with ~ 100 pc resolution, the community is rightfully searching for better treatments for sub-resolution physics that do not add too many tunable parameters to an already complex problem. Only when a self-consistent framework is implemented that appropriately describes the physical processes between gas, stars, and MBHs at a given resolution can we acquire any insight from the simulation about high- z MBHs.

In this work, we introduce a new breed of simulation that is aimed at resolving the “mismatch” between the best resolution in the field and the physics models used.

(1) First, for MBH physics, we improve the framework that was first introduced in Kim et al. (2011). Our framework describes how the interstellar gas flows around and accretes onto a MBH using high-resolution adaptive mesh refinement (AMR). Rather than resorting only to a thermal feedback prescription, we employ two channels of MBH feedback: radiative feedback—photoionizing radiation traced via full three-dimensional adaptive ray tracing—and mechanical feedback—bipolar winds resolved in AMR (Section 2.3). Earlier or similar versions of this framework have been used to study co-evolution of a star-forming galaxy and its embedded MBH (Kim et al. 2011), evolution of MBHs in merging galaxies (Kim 2011), and the early growth of a MBH seed at $8 \lesssim z \lesssim 15$ (Aykutalp et al. 2014; Latif et al. 2018; Smidt et al. 2018), sometimes at very high resolution depicting the near-relativistic jets from a MBH seed accreting at super-Eddington rates (Regan et al. 2019). In particular, in Kim et al. (2011) our MBH framework proved rewarding in depicting a new mode of MBH feedback that locally suppresses star formation in the galaxy’s core and self-regulates its own growth by heating up the surrounding ISM.

(2) Second, for the physics of star-forming molecular clouds (SFMCs), we adopt and improve the framework established in Kim et al. (2013a, 2013b). Here, the framework describes radiation from each of $\sim 10^4$ SFMC particles—each of which represents a mass of $\gtrsim 10^3 M_\odot$ —by tracing the UV photons on the fly, as well as thermal supernovae feedback (Section 2.2). This means that our approach considers the early stellar feedback channels before the supernovae explode. Joined with high spatial resolution, this framework was successfully applied to a dwarf-sized galaxy to study how stellar radiation escapes SFMCs and the galaxy (Kim et al. 2013a), and how different life stages of SFMCs manifest themselves in a spatially resolved star formation relation between $H\alpha$ and H_2 surface densities (Kim et al. 2013b).

Using our framework aimed at self-consistently modeling MBH and SFMC physics, in this paper we study the interactions between different galactic ingredients of a high- z galaxy with high spatial resolution. With a MBH of mass $\gtrsim 10^6 M_\odot$ embedded in a $\sim 7 \times 10^{10} M_\odot$ halo at $z \sim 7.5$, we study a massive quasar-host—assuming that its MBH has already experienced a sizable early buildup (from $\sim 10^2 M_\odot$ to $\sim 10^6 M_\odot$). The novelty of our physics models means that we can shed light on aspects of galaxy-MBH evolution that previous approaches could not. We can also provide unique perspectives for the high- z MBH puzzle. An example would be how interstellar gas is consumed by two competing channels—star formation and MBH accretion—in the vicinity of a MBH. As the discussion in the present paper will make clear, we found that radiation from young stars, combined with radiation and winds from the MBH, helps to retain interstellar gas near the MBH, which might otherwise have been rapidly consumed by runaway star formation. The unused gas is then available as a fuel for the MBH, increasing its growth rate when compared with the run without stellar radiation feedback (see Section 3.2 for a detailed discussion). This example demonstrates that the interplay between gas, stars, and MBHs that were never realized in previous simulations may contain critical information about the expeditious growth of MBHs at high z .

The remainder of the paper is organized as follows. In Section 2, we briefly explain the simulation framework, the physics models, and the initial condition of the experiment. Next, Sections 3 and 4 are devoted to the results and discussion of the reported simulations, with particular emphases on the interplay between gas, SFMCs, and a MBH. Finally, in Section 5 we summarize our findings and implications, with discussions on the future direction of the project.

2. Methodology

Our numerical experiment is designed to depict a galactic halo of $\sim 7 \times 10^{10} M_\odot$ at $z \sim 7.5$ with an embedded MBH seed of $\gtrsim 10^6 M_\odot$. The simulations presented here were run with the ENZO code (Bryan & Norman 1997; Norman & Bryan 1999; Norman et al. 2007; Bryan et al. 2014).⁷ Our variant of ENZO includes all physics relevant in a galaxy-scale simulation, as well as improved versions of MBH physics and SFMC physics modules (improved from Kim et al. 2011, 2013a, 2013b, respectively). For completeness and the reproducibility of the experiment, we review the framework’s key features focusing on the improvements when compared with our earlier studies.

2.1. Hydrodynamics, Refinement, and Cooling

We employ the ZEUS hydrodynamics solver to evolve the collisional fluid (Stone & Norman 1992a, 1992b).⁸ The mass thresholds for gas and particles above which a cell is refined depend on a refinement level l as

$$M_{\text{ref,gas}}^l = 2^{-0.446l} \times 4 \times (1/2^3)^5 \times \Omega_b \rho_0 \Delta x_0^3 \quad (1)$$

⁷ The website is <http://www.enzo-project.org/>.

⁸ We find that the typical runtime parameter combinations of the PPM solver in ENZO often stall or fall back to the lower-order-accurate solvers, especially when we combine the on-the-fly calculation of radiative feedback from SFMC and MBH particles, and the wind feedback from MBH particles. Thus, to keep the consistency in the numerical accuracy that we achieved, we employ a less-accurate but more stable ZEUS solver. However, we note that the more sophisticated subgrid physics we can include with ZEUS could justify our choice.

$$M_{\text{ref,part}}^l = 2^{-0.143l} \times 4 \times (1/2^3)^5 \times \Omega_m \rho_0 \Delta x_0^3 \quad (2)$$

where Δx_0 is the cell size at a root level, and $\rho_0 = 3H^2/8\pi G$ is the critical density of the universe. A factor $(1/2^3)^5$ is to refine all the cells in the first five nested levels. The Λ CDM cosmology that we adopt matches the one used to setup the initial condition (see Section 2.4) and is consistent with WMAP7+SNe+BAO: $\Omega_m = 0.272$, $\Omega_b = 0.0455$, and $H = 70.2 \text{ km s}^{-1}\text{Mpc}^{-1}$ (Komatsu et al. 2011). Readers may notice that our choice of M_{ref}^l refines the grids more on small scales (super-Lagrangian). With a root resolution of 128^3 in a $(60 \text{ comoving } h^{-1} \text{ Mpc})^3$ box, the finest mesh at $l = 14$ gives a maximal physical resolution $\Delta x_{14} = 4.79 \text{ pc}$ at $z = 7.5$, which is approximately in accord with the Jeans length for a dense gas clump of $n = 10^3 \text{ cm}^{-3}$ at $\sim 100 \text{ K}$. The corresponding Jeans mass, $2000 M_\odot$, is then used as a threshold for star formation at $l = 14$, above which the gas cell collapses to spawn a SFMC particle (see Section 2.2 and Kim et al. 2013a for more discussion). $M_{\text{ref,gas}}^{14} = 3000 M_\odot$ is chosen so that it is consistent with the above Jeans argument, while $M_{\text{ref,part}}^{14} = 1.13 \times 10^6 M_\odot$ is set to the mass of four finest dark matter particles.

The non-equilibrium chemistry module in ENZO tracks six species (H, H^+ , He, He^+ , He^{++} , e^-) and six collisional processes between them. Meanwhile, ENZO computes the primordial cooling rate by considering collisional excitation/ionization cooling, recombination cooling, Bremsstrahlung cooling, and CMB Compton cooling for hydrogen and helium (Anninos et al. 1997). When above 10^4 K , we add the metal cooling rate to the primordial rate, $\Delta\Lambda(Z) = \Lambda_{\text{net}}(Z) - \Lambda_{\text{net}}(0)$, where Λ_{net} is the net cooling rate tabulated in Sutherland & Dopita (1993). If below 10^4 K , then we use an approximated $\Lambda(T)$ found in Koyama & Inutsuka (2002) with corrections noted in Vázquez-Semadeni et al. (2010). Unlike Kim et al. (2011), metagalactic UV background radiation is not included because we consider one of the first, massive galaxies at $z \gtrsim 7.5$ that generates its own cosmological H II region and is unaffected by radiation from other galaxies.

2.2. SFMC Physics

Now we summarize our SFMC physics model, which is improved from a version tested in Kim et al. (2013a, 2013b). The finest gas cell of size Δx_{14} and density ρ_{gas} produces a SFMC particle of initial mass $M_{\text{MC}}^{\text{init}} = \epsilon_* \rho_{\text{gas}} \Delta x_{14}^3$ with efficiency $\epsilon_* = 0.5$ (a value established and extensively tested in connection with the other star formation criteria in earlier studies; see Kim et al. 2011, 2013a, 2013b) when (a) the proton number density exceeds the threshold $n_{\text{thres}} = 10^3 \text{ cm}^{-3}$, (b) the velocity flow is converging, (c) the cell's cooling time is shorter than the gas dynamical time, and (d) the particle produced has at least $M_{\text{thres}} = 1000 M_\odot$. Because the gas is instantly converted to a particle when a gas cell of $M_{\text{thres}}/\epsilon_* = 2000 M_\odot$ becomes Jeans unstable, the gas mass in the finest cell never reaches the refinement threshold $M_{\text{ref,gas}}^{14} = 3000 M_\odot$ as described in Section 2.1, which ensures the consistency between the SFMC formation machinery and the refinement criteria (Section 2.1 and Kim et al. 2013a for more discussion). The SFMC particle thus represents a self-gravitating star-forming cloud decoupled from the rest of the gas.⁹

⁹ Readers should note that SFMC particles could form even in the cell where the MBH sits. See Section 3.2 for related discussion.

Once created, a SFMC particle describes feedback from a population of stars in it, with its mass evolving as

$$M_{\text{MC}}(t) = \begin{cases} M_{\text{MC}}^{\text{init}} & \text{if } T/\text{Myr} < 4 \\ M_{\text{MC}}^{\text{init}} \left[1 - 0.8 \left(\frac{T-4}{40-4} \right) \right] & \text{if } 4 < T/\text{Myr} < 40 \\ 0.2 M_{\text{MC}}^{\text{init}} & \text{if } T/\text{Myr} > 40 \end{cases} \quad (3)$$

where $T = t - t_{\text{cr}}$ is the particle age in Myr with particle creation time t_{cr} . This formulation entails different life stages of a SFMC particle. (a) At its birth, $0.24 M_{\text{MC}}^{\text{init}}$ is considered to have instantly turned into stars. The rest, $0.76 M_{\text{MC}}^{\text{init}}$, never participates in star formation, modeling inefficient star formation in molecular clouds (e.g., Krumholz & Tan 2007; Murray et al. 2010). (b) Among the initial stellar mass of $0.24 M_{\text{MC}}^{\text{init}}$, 83% ends up forever locked in the particle as permanent stellar mass, $M_* = 0.20 M_{\text{MC}}^{\text{init}}$. (c) The remaining 17%, or $0.04 M_{\text{MC}}^{\text{init}}$, represents stars massive enough to ignite Type II SNe that continuously inject thermal energy from $T = 4$ to 40 Myr .¹⁰ During this time, $M_{\text{MC}}^{\text{init}} - M_* = 0.8 M_{\text{MC}}^{\text{init}}$ is gradually released back to the ISM, along with 3.75×10^{-5} of the rest mass energy of M_* in thermal form. This energy corresponds to $2 \times 10^{51} \text{ erg}$ per every $30 M_\odot$ of permanent stellar mass M_* produced. 2% of the ejecta mass is considered as metals. It is noted that the energy and duration of our thermal feedback model updates those in Kim et al. (2011) or Kim et al. (2013a, 2013b), and roughly matches previous studies such as Ceverino & Klypin (2009, based on STARBURST 99 estimation).

In addition to thermal supernovae, SFMC particles with ages $T < 100 \text{ Myr}$ may heat up the surrounding ISM by emitting UV photons. Using ENZO's radiative transfer machinery described in previous work (e.g., Abel & Wandelt 2002; Wise & Abel 2011), as well as in Kim et al. (2011, 2013a, 2013b), we perform an explicit three-dimensional ray tracing calculation to evolve the radiation fields throughout the galaxy. The radiation luminosity is assigned to each SFMC particle by

$$L_{\text{MC}}(t) = q_{\text{MC}} E_{\text{ph}} M_{\text{MC}}(t) \quad (4)$$

where $q_{\text{MC}} = 6.3 \times 10^{46} \text{ photons s}^{-1} M_\odot^{-1}$ is the lifetime-averaged ionizing luminosity (Murray & Rahman 2010), and $E_{\text{ph}} = 16.0 \text{ eV}$ is the mean monochromatic energy per photon (Whalen & Norman 2006).¹¹ Initially, 12×4^3 rays are isotropically cast from the particle with $L_{\text{MC}}(t) dt_{\text{ph}} / (E_{\text{ph}} \cdot 12 \times 4^3)$ photons per ray. Here, the radiation timestep dt_{ph} is adaptively set by the code, which is comparable with the finest hydrodynamic timestep most of the time (Wise & Abel 2011). Each ray is split into four child rays whenever the area associated with a ray becomes larger than $0.2(\Delta x)^2$ of a local cell, and is traced until the edge of the computational

¹⁰ $0.04 M_{\text{MC}}^{\text{init}}$ corresponds to 17% of the initial stellar mass assuming that massive stars with $> 8 M_\odot$ commence SNe II in a Salpeter (1955) initial mass function between 0.1 and $300 M_\odot$. Note that the mass evolution Equation (3) and the duration of SNe are updated from Kim et al. (2013a).

¹¹ Our choice to use $M_{\text{MC}}(i, t)$ in estimating $L_{\text{MC}}(t)$ rather than the stellar mass is to approximately compensate for various other early channels of SFMC feedback beyond photoionization, such as protostellar outflows and stellar winds. See Kim et al. (2013a) for complete discussion.

domain.¹² Photons in the ray affect the surrounding ISM, first by ionizing hydrogen with the rate of

$$k_{\text{ph,H}} = \frac{P_{\text{in}}(1 - e^{-\tau_{\text{H}}})}{n_{\text{H}}(\Delta x)^3 dt_{\text{ph}}} \quad (5)$$

where P_{in} is the number of incoming photons and $\tau_{\text{H}} = n_{\text{H}}\sigma_{\text{H}}(E_{\text{ph}})dl$ is the optical depth of a cell; and second by heating the gas with the excess energy above the ionization threshold with the rate of

$$\Gamma_{\text{H}} = k_{\text{ph,H}}(E_{\text{ph}} - 13.6 \text{ eV}). \quad (6)$$

UV radiation is the only feedback channel before the thermal supernovae feedback kicks in at $T = 4$ Myr. It is worth noting two points here: (a) although both hydrogen and helium are tracked in the chemistry module, only hydrogen is considered in photoionization and photoheating calculations (as in Kim et al. 2013a); and (b) we do not consider radiation pressure on gas—either by hydrogen-ionizing UV photons (unlike Kim et al. 2013a), or by multiply scattered IR photons (e.g., Hopkins et al. 2014, 2018). Including the radiation pressure might strengthen the SFMC feedback, even though controversies exist about the exact level of enhancement (e.g., Krumholz & Thompson 2013).

2.3. MBH Physics

We plant a MBH seed at the target galaxy’s center as a source of gas accretion and feedback. The rate of accretion is estimated with the Bondi–Hoyle formula (Bondi 1952) as

$$\dot{M}_{\text{BH}} = \frac{4\pi G^2 M_{\text{BH}}^2 \rho_{\text{B}}}{c_{\text{s}}^3} \quad (7)$$

where M_{BH} is the mass of the MBH, c_{s} is the gas sound speed of the cell in which the MBH resides, and ρ_{B} is the density at the Bondi radius R_{B} . When $R_{\text{B}} = 2GM_{\text{BH}}/c_{\text{s}}^2 \simeq 86 \text{ pc} (M_{\text{BH}}/10^6 M_{\odot})(c_{\text{s}}/10 \text{ km s}^{-1})^{-2}$ is resolved with $\Delta x_{14} (=4.79 \text{ pc at } z = 7.5)$ around the MBH,¹³ ρ_{B} is extrapolated from the density ρ_{gas} of the cell the MBH is located in, as

$$\rho_{\text{B}} = \rho_{\text{gas}} \cdot \min \left[\left(\frac{R_{\text{B}}}{\Delta x_{14}} \right)^{-1.5}, 1.0 \right] \quad (8)$$

following Kim et al. (2011) and Wang et al. (2010). The gas accreting onto the MBH is subtracted uniformly from the cells within R_{B} . Notice that in Equation (7) we do not include an empirical boost factor (similar to Kim et al. 2011 and other recent efforts by e.g., Weinberger et al. 2017 and Trebitsch et al. 2018).

¹² To speed up the calculation multiple measures are placed in the ray tracing machinery: (a) the photon luminosities $L_{\text{MC}}(t)$ are assigned only to the SFMCs that are within the virial radius of the target galaxy (15.1 proper kpc from the galactic center at $z \sim 7.5$, or 128.2 comoving kpc; see Section 2.4); (b) two SFMC particles are merged if separated by less than 16 proper pc in space and 0.1 Myr in creation time, in a way that conserves mass and momentum; (c) a ray is no longer split when it is more than 3 kpc from the source; and (d) two rays are merged if distances from the sources are more than 8 times the separation between the ray sources.

¹³ Our MBH is almost always sitting at the finest refinement level with a cell width Δx_{14} because it is located at the peak of gas distribution near the galactic center. This allows us to resolve the gas flow around the MBH with our best resolution, without necessarily requiring the cells around the MBH to be successively refined down to the finest level (as in Kim et al. 2011).

Nor do we impose the Eddington accretion limit (similar to other previous studies by e.g., Lupi et al. 2016). These two considerations are often critical—and controversial—in estimating the growth rate of a MBH in a cosmological timescale. But not so critical in the present study, in which our focus is to examine the interaction of a MBH and its host for a relatively short time (for ~ 25 Myr; see Section 2.4), not the *absolute* value of the MBH mass increase.¹⁴ By the same token, our choice of a MBH seed mass $1.8 \times 10^6 M_{\odot}$ is not very crucial either, but simply designed to induce substantial gas accretion—and feedback thereafter—by the MBH. This is in line with the argument for a $8 \times 10^5 h^{-1} M_{\odot}$ black hole seed adopted in Weinberger et al. (2017) (see more discussion in Section 2.4).

Once starting to accrete gas from its neighborhood, the total feedback energy rate by the MBH particle is given as

$$L_{\text{BH}}(t) = \epsilon_{\text{r}} \dot{M}_{\text{BH}}(t) c^2 \quad (9)$$

where $\epsilon_{\text{r}} = 0.1$ is the conversion factor from the rest mass energy of accreting gas to the MBH’s feedback energy (Shakura & Sunyaev 1973). In the reported experiment, two channels of MBH feedback are implemented: radiative and mechanical. Each channel contributes equally (i.e., $0.5 L_{\text{BH}}(t)$ each) to the total feedback energy. To begin with, for the transfer calculation of radiation from the MBH, we assume that the UV luminosity of the MBH is proportional to its bolometric luminosity as

$$L_{\text{BH,UV}}(t) = 0.5 f_{\text{UV}} L_{\text{BH}}(t) \quad (10)$$

with a proportionality coefficient $f_{\text{UV}} = 0.1$. Our choice of f_{UV} is broadly consistent with the estimate given in Bieri et al. (2017) using the Sazonov et al. (2004) active galactic nuclei (AGNs) spectrum (e.g., $f_{\text{UV1}} = 0.079$ in Trebitsch et al. 2018). As in the case of SFMC photons (Section 2.2), monochromatic energy of $E_{\text{ph}} = 16.0 \text{ eV}$ is used for photon rays. Note that our E_{ph} is in line with the luminosity-weighted average in the energy band of the Sazonov et al. (2004) spectrum that contributes to the ionization of neutral hydrogen ($E_{\text{ph}} = 18.0 \text{ eV}$ in Trebitsch et al. 2018).¹⁵ When the rays travel through the gas cells, the photons interact with hydrogens via photoionization and photoheating, Equations (5) and (6), respectively. As in SFMC photons, we neglect radiation pressure by MBH photons, which is conservative because its inclusion would have furthered the feedback effect (e.g., Debuhr et al. 2011; Bieri et al. 2017; Costa et al. 2018).

In addition to the radiation channel, a MBH particle can launch bipolar winds by injecting mass and momentum in its vicinity. The kinetic power of these subrelativistic winds, as we introduce in the cells that are $2 \Delta x_{14}$ away from the MBH (see Figure 2 of Kim et al. 2011 for a schematic description), depends on the accretion rate as

$$P_{\text{w}} = 0.5 \epsilon_{\text{w}} L_{\text{BH}}(t) = \frac{1}{2} \dot{M}_{\text{w}} v_{\text{w}}^2 \quad (11)$$

¹⁴ Surely, the Bondi accretion estimate will need to be reconsidered in an even higher-resolution simulation. See Section 5.2 for more discussion.

¹⁵ Therefore, our formulation implies that the ISM surrounding the MBH is either optically thin to the photons in other energy bands (e.g., when $E \gg 16.0 \text{ eV}$) or negligibly affected by them (e.g., when $E \ll 16.0 \text{ eV}$). We implicitly assume that only the UV portion of the AGN spectrum can thermally couple with the surrounding ISM.

where ϵ_w encapsulates how much of the mechanical energy of a MBH is turned into winds at the scale we introduce them in the simulation ($\sim 2 \Delta x_{14}$), and \dot{M}_w is the mass ejection rate of the winds. With conservative choices of $\epsilon_w = 10^{-4}$ and $\eta_w = \dot{M}_w / \dot{M}_{\text{BH}} = 0.1$ (based on the prior investigation in Kim et al. (2011) and an one-dimensional study in e.g., Ciotti et al. 2009), the wind velocity v_w when introduced in the simulation is determined by

$$v_w = c \left(\frac{\epsilon_w \epsilon_r}{\eta_w} \right)^{1/2} = 3000 \text{ km s}^{-1} \quad (12)$$

for $\epsilon_r = 0.1$. We intermittently inject the ejecta in a form of collimated bipolar winds of width $5 \Delta x_{14}$ (Figure 2 of Kim et al. 2011) every time the accumulated ejecta mass, $\Sigma \dot{M}_w dt$, exceeds a $300 M_\odot$ threshold. The direction of the winds is parallel and antiparallel to the total angular momentum of the accreted gas up to that point, with an added leeway angle of $< 10^\circ$.¹⁶ The velocities of the surrounding cells are then found by averaging the momenta over the injected wind masses and the preexisting cell masses. As in the ejecta from SFMCs, 2% of the MBH wind mass is considered as metals because we hope to account for unresolved star formation below resolution occurring in the cell hosting the MBH.

2.4. Initial Condition and Simulation Suite

Since quasars are very rare at $z \gtrsim 7$, a large simulation box is necessary. Meanwhile, numerical resolution of $< 10 \text{ pc}$ is essential to resolve the characteristic SFMC scale and the gas flow around a $\gtrsim 10^6 M_\odot$ MBH. This high dynamic range is achieved by the “zoom-in” initial condition generator MUSIC that uses an adaptive multi-grid Poisson solver (Hahn & Abel 2011), and by the AMR code ENZO. In particular, we use a set of MUSIC parameters that describes a halo that eventually grows into $\sim 10^{13} M_\odot$ group at $z = 0$ with a relatively quiescent merger history. This is one of the publicly available cosmological initial conditions identified in a $(60 \text{ comoving } h^{-1} \text{ Mpc})^3$ box by the AGORA High-resolution Galaxy Simulations Comparison Project (i.e., initial condition tagged “1e13q”; Kim et al. 2014, 2016).¹⁷ Here, a flat Λ CDM cosmology that is consistent with WMAP7 + SNe + BAO is assumed: $\Omega_m = 0.272$, $\Omega_\Lambda = 0.728$, $\sigma_8 = 0.807$, $n_s = 0.961$, and $H_0 = 70.2 \text{ km s}^{-1} \text{ Mpc}^{-1}$ (Komatsu et al. 2011, see Section 2.1). The primary progenitor of our target halo at $z \sim 7.5$ is determined as a halo of $M_{\text{vir}} \simeq 7 \times 10^{10} M_\odot$ and $M_* \simeq 8 \times 10^9 M_\odot$ with a virial radius $R_{\text{vir}} = M_{\text{vir}}^{1/3} (H^2 \Omega_m \Delta_c / 2G)^{-1/3} \simeq 15 \text{ kpc}$ (with $\Delta_c = 200$).¹⁸ With a 128^3 root grid and a series of five nested child grids of twice finer resolution each, the equivalent unigrid resolution at level $l = 5$ is 4096^3 (Figure 1).

The simulation is first run with a maximal resolution of $163.0 \text{ comoving pc}$ from $z = 100$ to 7.8 (i.e., maximum

refinement level $l = 12$ with $\Delta x_{12} = 18.5 \text{ pc}$ at $z = 7.8$). Then, in the next $\sim 40 \text{ Myrs}$ from $z = 7.8$ to 7.5 , we simulate the target halo with additional two levels of refinement ($\Delta x_{14} = 4.79 \text{ pc}$ at $z = 7.5$) with the refinement strategy and SFMC physics described in Sections 2.1 and 2.2, respectively, but without an accreting MBH. This run sets up a relaxed, well-resolved high- z galaxy at $z = 7.5$ with which we vary physics to build a suite of simulations (Figures 1 and 2). Then finally, at $z = 7.5$ we restart the calculation with a $1.8 \times 10^6 M_\odot$ MBH implanted at the target galaxy’s center, while turning on the MBH physics discussed in Section 2.3 to run for another $\sim 25 \text{ Myr}$ until $z = 7.3$ (Sim-SRTF+BH). For comparison, another simulation is run with similar physics inputs but without the *radiative* channel of SFMC feedback (Sim-STF+BH). We also have a control run with all the SFMC physics but without a MBH (Sim-SRTF). Table 1 summarizes the suite of simulations we perform. Note that the production simulations’ run time, $\sim 25 \text{ Myr}$, is of the order of the Salpeter timescale, τ_{Salpeter} , which is a characteristic timescale for a black hole growth at the Eddington accretion limit.

Two points about our experiment are noted. (a) By applying high-resolution refinement only well into the galaxy’s evolution, we save the computational expense to simulate the galaxy for a galactic dynamical time, but focus instead on the interaction of a MBH and its neighborhood for a typical lifetime of SFMCs or a rotational timescale of the galactic core region. (b) Thus, given a relatively short simulation time, we choose a slightly higher MBH seed mass for the halo mass, in an attempt to observe substantive effect by the MBH in the galactic inner region—a reasoning similar to Weinberger et al. (2017). Our MBH seed mass of $1.8 \times 10^6 M_\odot$ assumes a sizable prior buildup from $\sim 10^2 M_\odot$ to $\sim 10^6 M_\odot$ before $z = 7.5$. Consequently, the reported results should not be regarded as a general picture of MBHs at this redshift (for more discussion on the seed mass, see Section 2.3).

3. Results

The reported simulations and analyses were performed on various computational resources including the *Happiness* cluster at Seoul National University and the *Pleiades* cluster at the NASA Ames Research Center, among others. Toward the end of the simulation at $z = 7.3$, each simulation snapshot typically contains a total of $\sim 2 \times 10^8$ computational elements: $\sim 1.2 \times 10^8$ particles (dark matter, SFMC, MBH) and $\sim 9 \times 10^7$ gas cells in $\sim 4 \times 10^3$ grid patches. With measures to reduce the number of radiation sources (see footnote 6), the radiation transfer module in our code typically handles $\lesssim 3 \times 10^4$ ray-emitting sources in Sim-SRTF+BH and Sim-SRTF. We now analyze the three simulations listed in Table 1 to examine the interplay between the newly introduced SFMC and MBH physics. In all of the subsequent analyses, we utilize a code-independent analysis platform yt (Turk et al. 2011).¹⁹

3.1. Stellar and MBH Feedback Suppress Runaway Star Formation Locally

Comparing a suite of quasar-host simulations carried out with high spatial resolution ($\Delta x_{14} = 4.79 \text{ pc}$ at $z = 7.5$) and high fidelity physics, we are able to investigate how and how much stellar (SFMC) feedback suppresses star formation in the

¹⁶ The random leeway angle of $< 10^\circ$, which was absent in Kim et al. (2011), is introduced to broaden the area affected by the MBH winds.

¹⁷ The website is <http://www.AGORAsimulations.org/>. This particular IC, “1e13q”, has been used in several studies such as Fiacconi et al. (2016).

¹⁸ The high stellar mass of our target halo at $z \sim 7.5$ is due to an efficient star formation prescription adopted during the lower-resolution phase when making the target galaxy (see next paragraph). As will be discussed in Section 4.1, this stellar mass is roughly around the critical value above which MBHs start to grow more rapidly (e.g., Dekel et al. 2019).

¹⁹ The website is <http://www.yt-project.org/>.

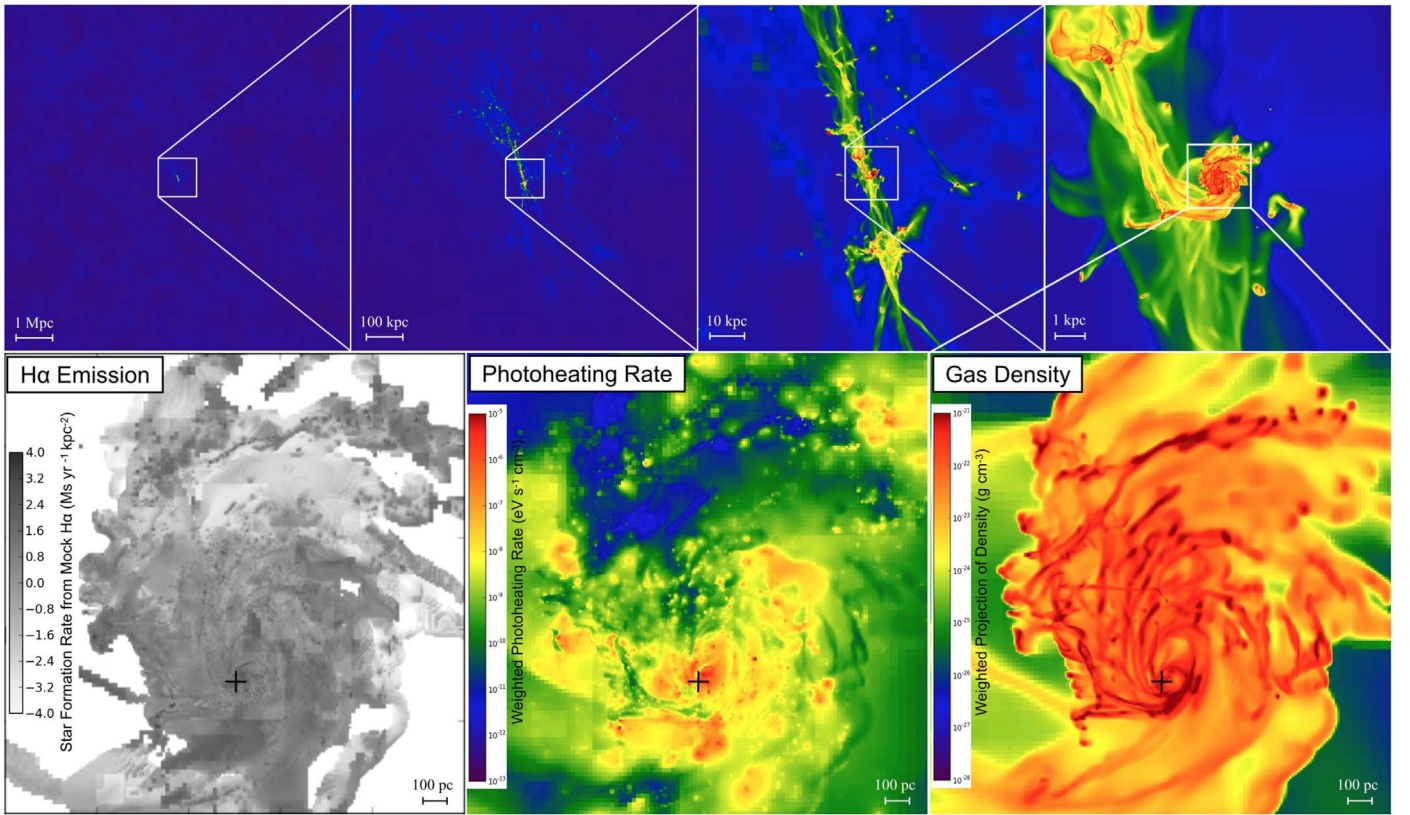


Figure 1. Overview of the target galaxy in a halo of total mass $\sim 7 \times 10^{10} M_{\odot}$ in our experiment at $z = 7.65$. Clockwise from top left to bottom right: projected gas densities at large to small scales seen from a face-on angle. Bottom middle: projected photoheating rate density calculated by ray tracing the UV photons from radiating SFMCs. Bottom left: star formation rate surface density estimated from mock H α emission (Kim et al. 2013b). This halo eventually grows into a $\sim 10^{13} M_{\odot}$ group at $z = 0$ (see Section 2.4). The high-resolution, full color version of this figure is available online and at <http://www.jihoonkim.org/>.

vicinity of a MBH, and change the ISM structure of a quasar-host galaxy. This will lead us to a better picture of how MBHs might have accumulated their masses in the high- z universe (to be discussed in Section 3.2).

Figure 3 overviews our target galaxy at $z = 7.3$ in various quantities in a $(1 \text{ kpc})^2$ field of view from the galactic edge-on angle. First, sliced density and temperature plots (2nd and 3rd rows) exhibit the impact of bipolar winds by the MBH (mechanical feedback) that blow surrounding gas away in Sim-SRTF+BH and Sim-STF+BH, leading to mushroom-shaped hot bubbles above and below the disk plane. We find that the energetic outflows driven by the MBH affect most critically the gas right above and below the disk, but not so much the gas *on* the disk. Meanwhile, the projected photoheating rates in the gas (4th row) reveal how many photons have escaped the dense gas layer right next to the photon sources such as SFMCs and MBHs, and then affect the interstellar gas in the galaxy. UV radiation from SFMCs and/or the MBH helps to heat up the gas in Sim-SRTF+BH and Sim-SRTF, while this heating is negligible in Sim-STF+BH (note that only the single MBH radiates photons in the latter case).

Our qualitative observations can be checked in the radial profiles in Figure 4 of temperature and radial velocity in the inner core of the galaxy. The left-hand panel of Figure 4 shows the mass-weighted radial profiles of gas temperature. Within a $\sim 100 \text{ pc}$ sphere centered on the MBH, the photoheating radiation from (mostly) young SFMCs helps to heat the gas up to $\sim 10^5 \text{ K}$ in Sim-SRTF+BH and Sim-STF—by making

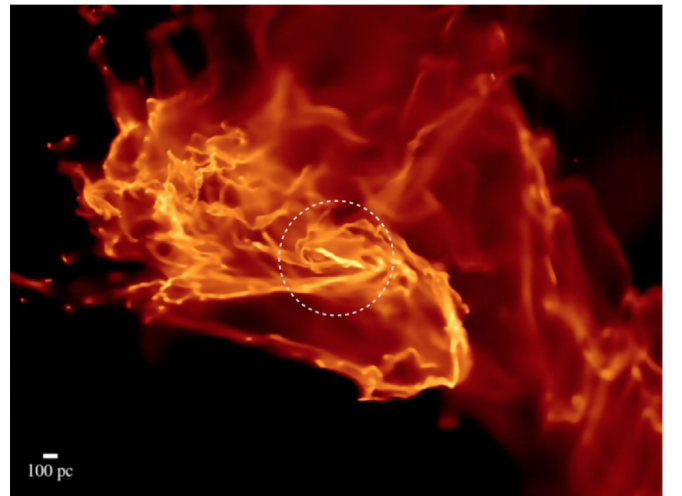


Figure 2. A snapshot of the target galaxy at $z = 7.3$ (Sim-SRTF+BH). The white dashed circle in the middle denotes the target galaxy’s inner disk (seen from an edge-on angle; see also Figure 3), which harbors a central MBH. For more information about the target galaxy, see Section 2.4 or the caption of Figure 1.

gas densities lower and cooling times longer, thus the SN feedback more efficient (so the SN ejecta cools more slowly in the presence of a radiation field). The nearly constant temperature of $\sim 10^4 \text{ K}$ for Sim-STF+BH indicates that the

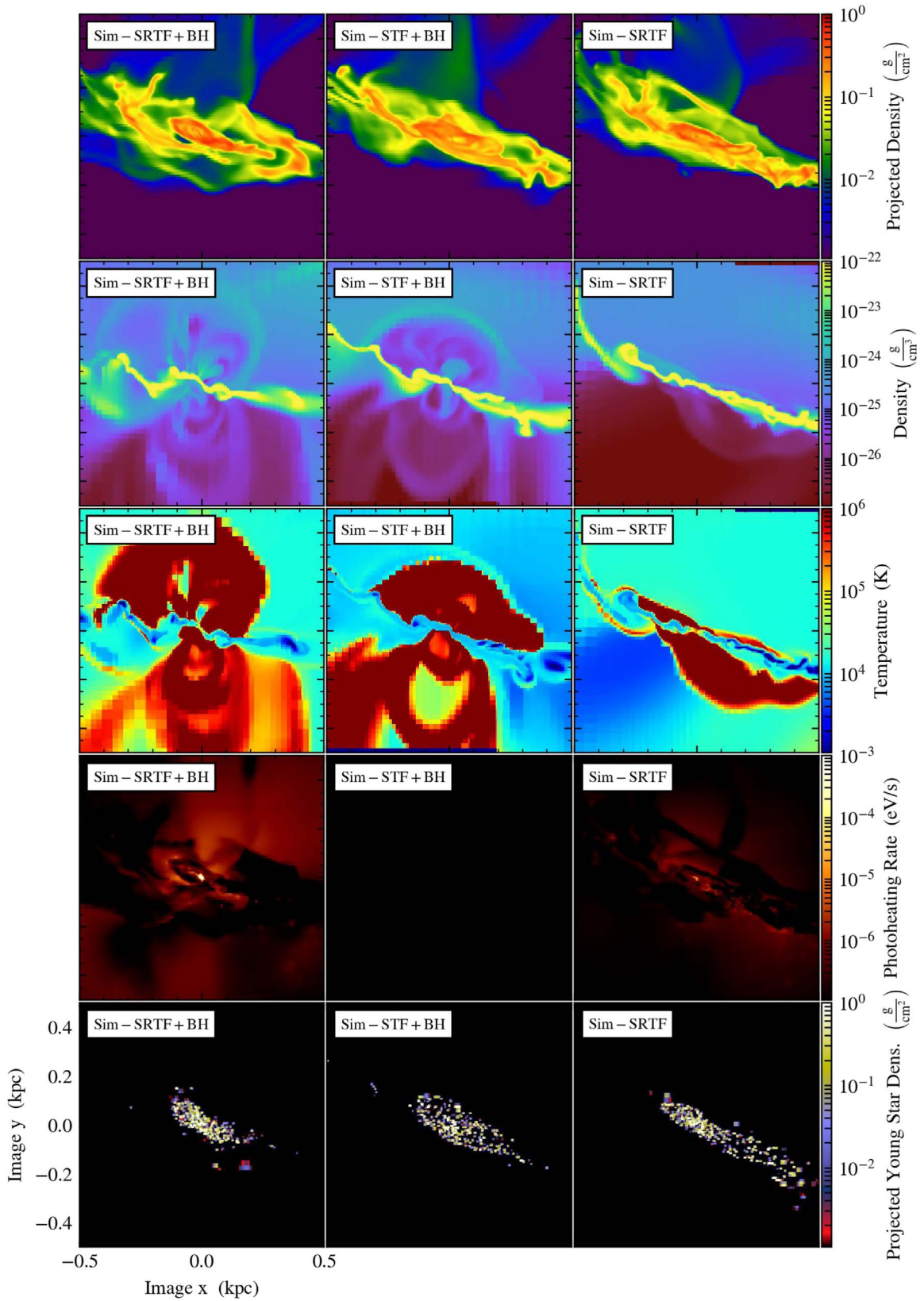


Figure 3. Overview of our simulation suite for a quasar-host galaxy with varying input physics, at the end of the run at $z = 7.3$ in a $(1 \text{ kpc})^2$ box. Shown here are (from top to bottom row) gas surface density, sliced density, sliced temperature, projected photoheating rate (density-weighted), and young stellar surface density (age $< 3 \text{ Myr}$), for the runs with thermal/radiative SFMC feedback and mechanical/radiative MBH feedback (left-hand column; “Sim-SRTF+BH”), similar but without radiative SFMC feedback (center column; “Sim-STF+BH”), and without a MBH (right-hand column; “Sim-SRTF”). See Table 1 and Section 2.4 for more information about the simulation suite. The line-of-sight in each panel is perpendicular to the angular momentum of the galactic disk (see also Figure 2). Bipolar bubbles created by MBH winds in Sim-SRTF+BH and Sim-STF+BH are prominent in sliced density and temperature (second and third row). Radiation from SFMCs and/or the MBH helps to heat up the gas in Sim-SRTF+BH and Sim-SRTF while such heating is negligible in Sim-STF+BH (4th row).

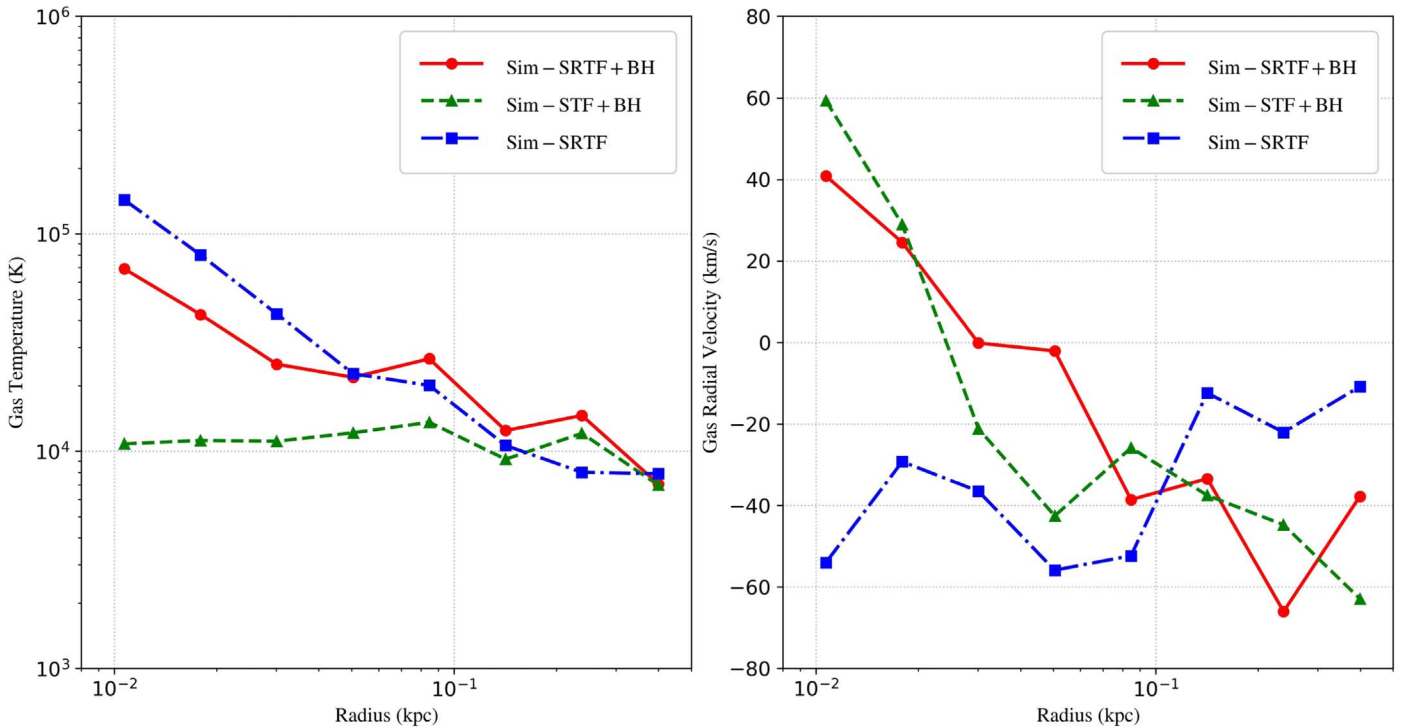


Figure 4. Mass-weighted radial profiles of temperature (left-hand) and radial velocity (right-hand) centered on the MBH at $z = 7.3$. The red solid line, green dashed line, and blue dotted–dashed line represent the runs with thermal/radiative SFMC feedback and mechanical/radiative MBH feedback (Sim-SRTF+BH), similar but without radiative SFMC feedback (Sim-STF+BH), and without a MBH (Sim-SRTF). See Table 1 and Section 2.4 for more information about the simulation suite. The radiation from SFMCs is responsible for the higher temperature of gas within < 100 pc from the galactic center in Sim-SRTF+BH and Sim-SRTF (left-hand). The wind feedback by the MBH blows the gas away from the center in Sim-SRTF+BH and Sim-STF+BH, a feature absent in Sim-SRTF (right-hand).

Table 1
Simulation Suite Description

Physics ^a		Sim-SRTF+BH	Sim-STF+BH	Sim-SRTF
SFMC formation ^b	(Section 2.2)	○	○	○
SFMC radiative feedback—ionizing radiation	(Section 2.2)	○	×	○
SFMC thermal feedback—supernovae explosion	(Section 2.2)	○	○	○
MBH accretion ^b	(Section 2.3)	○	○	×
MBH radiative feedback—ionizing radiation	(Section 2.3)	○	○	×
MBH mechanical feedback—bipolar winds	(Section 2.3)	○	○	×

Notes.

^a For detailed descriptions of the included physics, see referenced sections. ○ = included, × = not included.

^b SFMC = star-forming molecular cloud, MBH = massive black hole.

photons from the MBH alone (see Table 1) are not enough to raise the temperature above $\sim 10^4$ K, or fails to escape the thick layers of neutral hydrogen near the MBH (to be discussed again in Sections 3.2 and 4.2). It also suggests that the high temperatures in the galactic inner region in Sim-SRTF+BH and Sim-SRTF are due in the most part to radiation from SFMCs (see Section 4.2). The right-hand panel of Figure 4 shows a radial velocity profile evaluated from the location of the MBH, and how the gas dynamics in the galactic core region is changed by the MBH mechanical feedback. At large scales, there generally exist prominent gas inflows for a young, fast-growing galaxy like the one presented here, as are seen in all three simulations at outer radii ($\gtrsim 50$ pc). However, the MBH winds blow the gas away in the direction perpendicular to the disk plane in Sim-SRTF+BH and Sim-STF+BH, making the gas in the inner layer ($\lesssim 50$ pc) move outward *on average*. This happens despite the fact that the inflow on the galactic disk

plane is largely unaffected by the MBH feedback due to its thickness. Clearly, this is a feature that is absent in a run without the MBH feedback, Sim-SRTF.²⁰

Figure 5 shows in detail the structure of the ISM affected by stellar (SFMC) and MBH feedback within different enclosing radii. Each panel shows a density–temperature joint probability distribution function with a black, vertical dotted line denoting the density threshold for SFMC formation, n_{thres} (see Section 2.2). Without UV radiation from SFMCs, in Sim-STF+BH, cold dense gas instantly turns into SFMCs at n_{thres} leaving no gas over the threshold (region “A”). In contrast, the UV radiation from SFMCs and/or from the MBH helps to heat up the dense gas close to the

²⁰ Note that because radiation pressure is not considered in the reported simulations, MBH’s radiation alone would not drive outflows in Sim-SRTF+BH or Sim-STF+BH. Had we included the radiation pressure by the MBH—and SFMCs —, the gas outflows might have been enhanced.

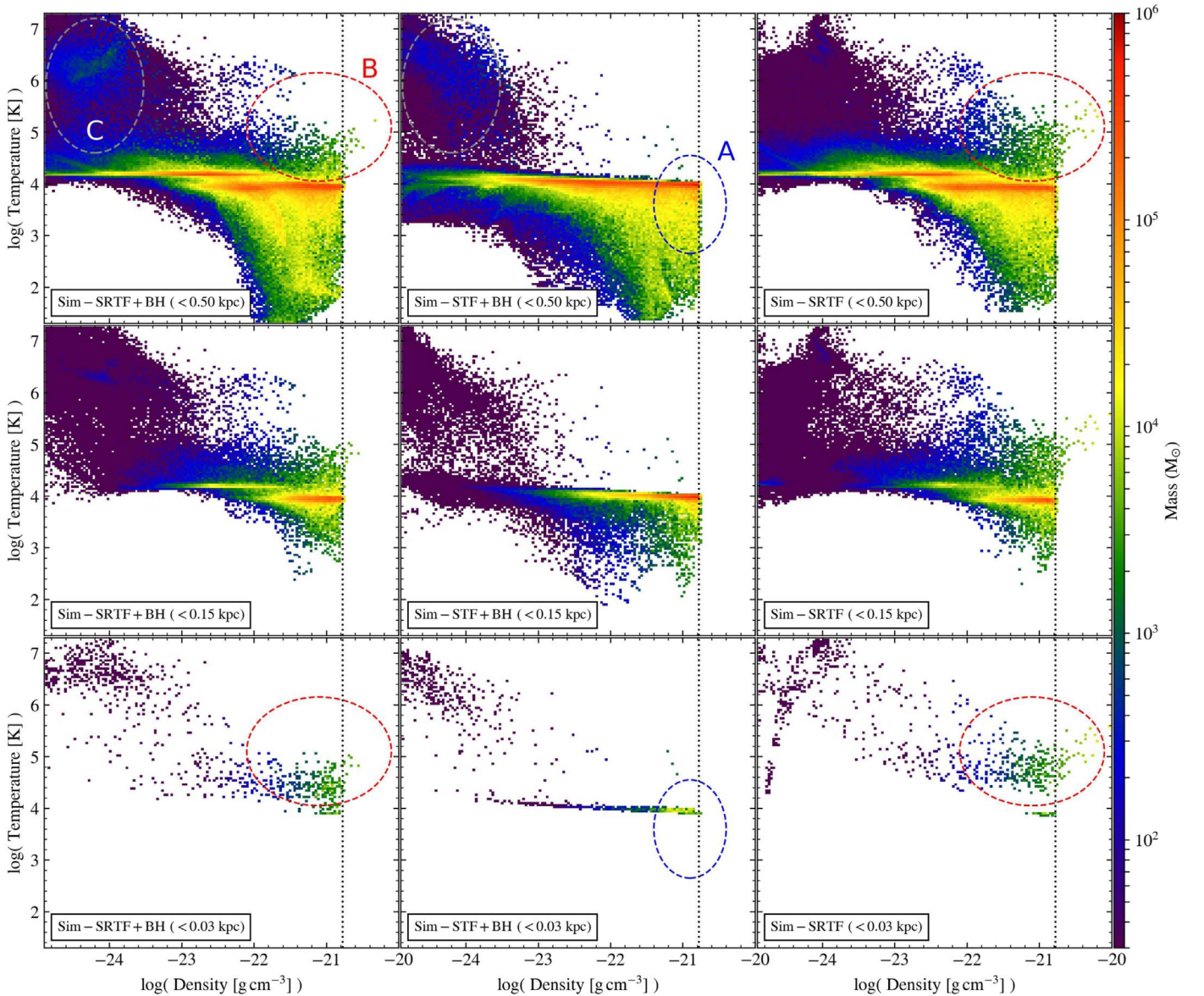


Figure 5. Density-temperature joint probability distribution functions (PDFs) in spheres of successively smaller radii (from top to bottom row) centered on the MBH at $z = 7.3$, for the runs with thermal/radiative SFMC feedback and mechanical/radiative MBH feedback (left-hand column; “Sim-SRTF+BH”), similar but without radiative SFMC feedback (center column; “Sim-STF+BH”), and without a MBH (right-hand column; “Sim-SRTF”). See Table 1 and Section 2.4 for more information about the simulation suite. Colors represent the gas mass in each two-dimensional bin. The star (SFMC) formation threshold density is denoted by a black dotted line in each panel (n_{thres} ; see Section 2.2). Without UV radiation from SFMCs, in Sim-STF+BH, cold dense gas turns into SFMCs at n_{thres} (region “A”). In contrast, UV radiation from SFMCs and/or from the MBH helps to heat up gas close to the MBH to $\sim 10^5$ K in Sim-SRTF+BH and Sim-SRTF making the gas stable against fragmentation (region “B”). Note also that the bipolar wind feedback from the MBH enhances and maintains the hot diffuse gas of $\gtrsim 10^6$ K in Sim-SRTF+BH and Sim-STF+BH (region “C”).

MBH to $\sim 10^5$ K in Sim-SRTF+BH and Sim-SRTF making the gas stable against fragmentation. Some hot, dense gas cells irradiated by SFMCs or the MBH still exist beyond the threshold because they do not turn into stars ($t_{\text{cool}} > t_{\text{dyn}}$; region “B”). The hot diffuse gas with $T \gtrsim 10^6$ K and $\rho \lesssim 10^{-23}$ g cm $^{-3}$ formed via supernova feedback is visible in all three simulations, but is particularly enhanced by the wind feedback from the MBH in Sim-SRTF+BH and Sim-STF+BH (region “C”).

As Figures 3–5 have illustrated, the hot temperature induced by the SFMC and MBH radiation, and the diverging flow of gas by the MBH-driven winds suppress the formation of SFMCs locally in Sim-SRTF+BH. The gas cells in the galactic center have harder time to fulfill all the SFMC formation conditions, such as a short cooling time ($t_{\text{cool}} < t_{\text{dyn}}$) and a

converging velocity flow ($\nabla \cdot v < 0$). Figure 6 shows the resulting distribution of new SFMCs (stellar mass) in the galaxy’s inner region. The red line depicts the suppressed star formation in Sim-SRTF+BH between $z = 7.5$ and 7.3 resulting in a considerable reduction of “new” stellar masses (SFMCs that were created between $z = 7.5$ and 7.3 after we vary the SFMC/MBH physics between different runs), in enclosed mass (left-hand panel) and radially averaged density (right-hand panel) profiles. As our previous findings suggest, note that only the combination of stellar (SFMC)+MBH radiation and MBH wind feedback leads to such suppression.

We caution that because the run times of the simulations reported here are relatively short owing to various numerical limitations (e.g., ~ 25 Myr for “Sim-SRTF+BH”), we have

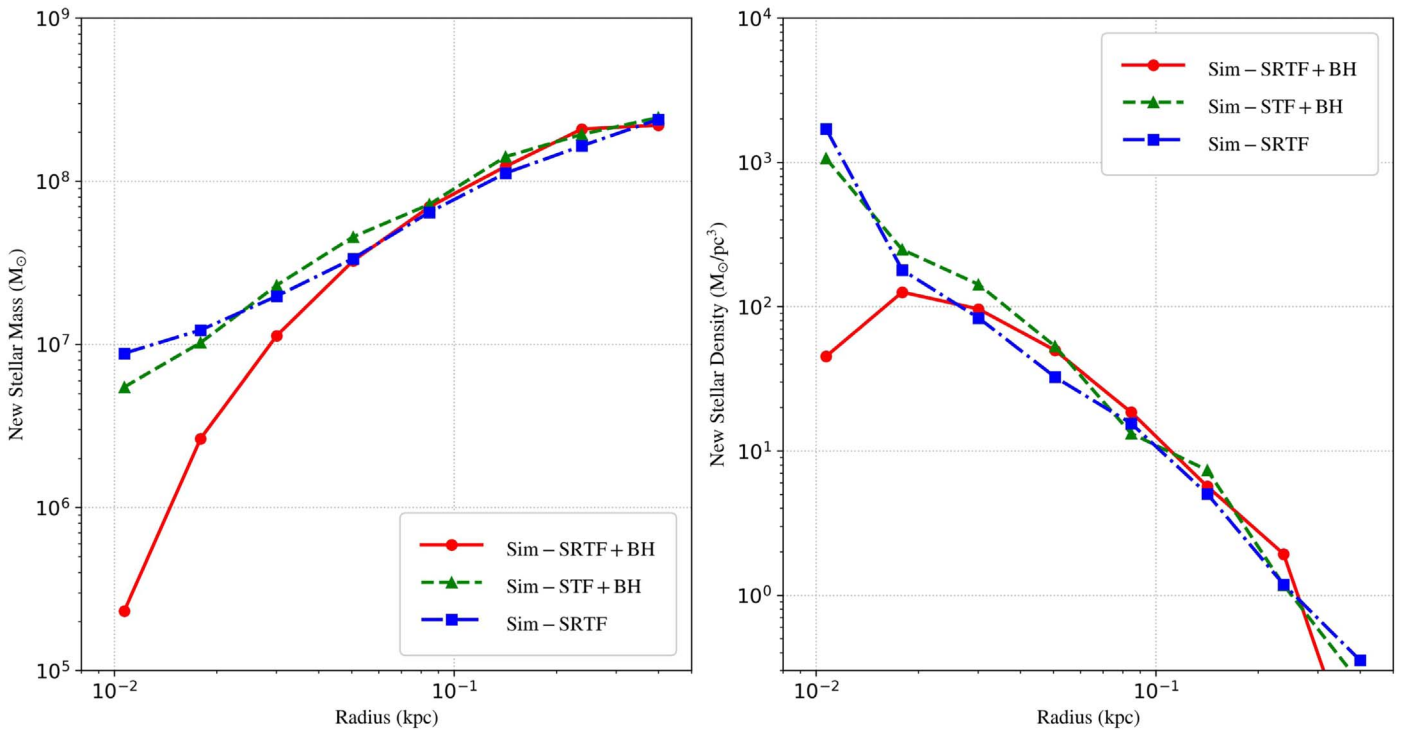


Figure 6. Enclosed mass (left-hand) and radially averaged density profiles (right-hand) of “new” SFMCs (those who were created between $z = 7.5$ and 7.3 after we vary the SFMC/MBH physics between different runs) in a 150 pc sphere centered on the MBH at $z = 7.3$. See Table 1 or the caption of Figure 4 for more information about the simulation suite. Locally suppressed star formation in Sim-SRTF+BH results in a considerable reduction of new stellar mass in the galactic core region. Considering the findings in Figures 3 to 5, note that only the combination of stellar (SFMC)+MBH radiation and MBH wind feedback leads to such suppression.

observed only the beginning of how SFMC and MBH feedback will transform the galaxy as a whole. An attempt to acquire a more complete picture of the galactic transformation—by advancing the simulation for a longer time with better optimizations—is currently being made (see Section 5.2).

3.2. Stellar and MBH Feedback Help the MBH Grow by Retaining the Fuel for Accretion

Now we specifically focus on how the MBH acquires its mass, and how SFMC and MBH feedback have affected its accretion process in our suite of simulations (Table 1). Figure 7 displays the gas accretion rate on to the central MBH (left-hand panels) and the formation rates of stars (SFMCs) that are located within 150 pc from the MBH at $z = 7.3$ (top right-hand panel), and within 30 pc (bottom right-hand panel). Combined with our findings in Figure 6, Figure 7 implies that the SFMC formation in Sim-SRTF+BH is suppressed mostly only within the galaxy’s inner core region ($\lesssim 50$ pc). The unused interstellar gas remains near the MBH which could otherwise have been rapidly consumed through runaway star formation (see also Figures 5 and 8). In the meantime, MBH accretion rate of Sim-SRTF+BH is continuously higher than that of Sim-STF+BH.²¹ Indeed, the MBH in Sim-SRTF+BH after just ~ 25 Myr grew by $2.9 \times 10^6 M_\odot$ with a growth rate of $0.113 M_\odot \text{yr}^{-1}$. This is approximately 1–3 times the Eddington rate for the MBH mass of $\sim 2 \times 10^6 M_\odot$ (bottom left-hand panel of Figure 7). Note that the Eddington limit is not imposed in our accretion estimation (see the related discussion in Section 2.3). By contrast, the MBH mass in Sim-STF+BH was increased by

$1.1 \times 10^6 M_\odot$ at the rate of $0.041 M_\odot \text{yr}^{-1}$. These observations strongly indicate that the unconsumed gas in Sim-SRTF+BH fuels the enhanced growth of the MBH when compared with Sim-STF+BH.

To take a deeper look into the neighborhood around the accreting MBH, in Figure 8 we display the snapshots of the target galaxy in boxes of $(300 \text{ pc})^3$ centered on the MBH at $z = 7.3$ from the face-on angle of its disk plane. In the analyses hereafter (for Figures 8–9), the disk is defined as a plane perpendicular to the angular momentum vector of the gas within a 150 pc radius. As seen in Figure 4, a core of hot gas above $\gtrsim 10^5$ K occupies the galaxy’s center in Sim-SRTF+BH and Sim-SRTF (2nd row). This hot core is created by radiation from mostly SFMCs, as discussed in Section 3.1, while such photoheating effect is nearly absent in Sim-STF+BH (3rd row; photons from the MBH rarely escapes the galaxy’s center most of the time in Sim-STF+BH due to thick layers of neutral hydrogen). And the “new” stellar density in the disk of Sim-SRTF+BH shows a sign of locally suppressed star formation in the core region when compared with Sim-STF+BH and Sim-SRTF (4th row; for the definition of “new” stellar mass, see the caption of Figure 8). As discussed in Section 3.1 and Figure 6, only the combination of stellar (SFMC)+MBH radiation and MBH winds leads to such suppression.

The relationship between the SFMC+MBH feedback and the state of the gas around the MBH can be nicely explained by the cylindrical profiles of the sound speed (measure of gas pressure) and the Toomre Q parameter (measure of gas stability) in Figure 9. In the left-hand panel, the high value of gas sound speed, $c_s \sim (k_B T / m_p)^{1/2}$, in Sim-SRTF+BH and Sim-SRTF is a direct consequence of photoheating radiation by SFMCs discussed in Figure 4. With this c_s , our slightly modified version of the Toomre Q parameter is displayed on

²¹ The elevated MBH accretion rate star formation rate at 740–745 Myr is thought to be related to a recent close encounter with a smaller galaxy. We hope to investigate this merging event in future research (see Section 5.2).

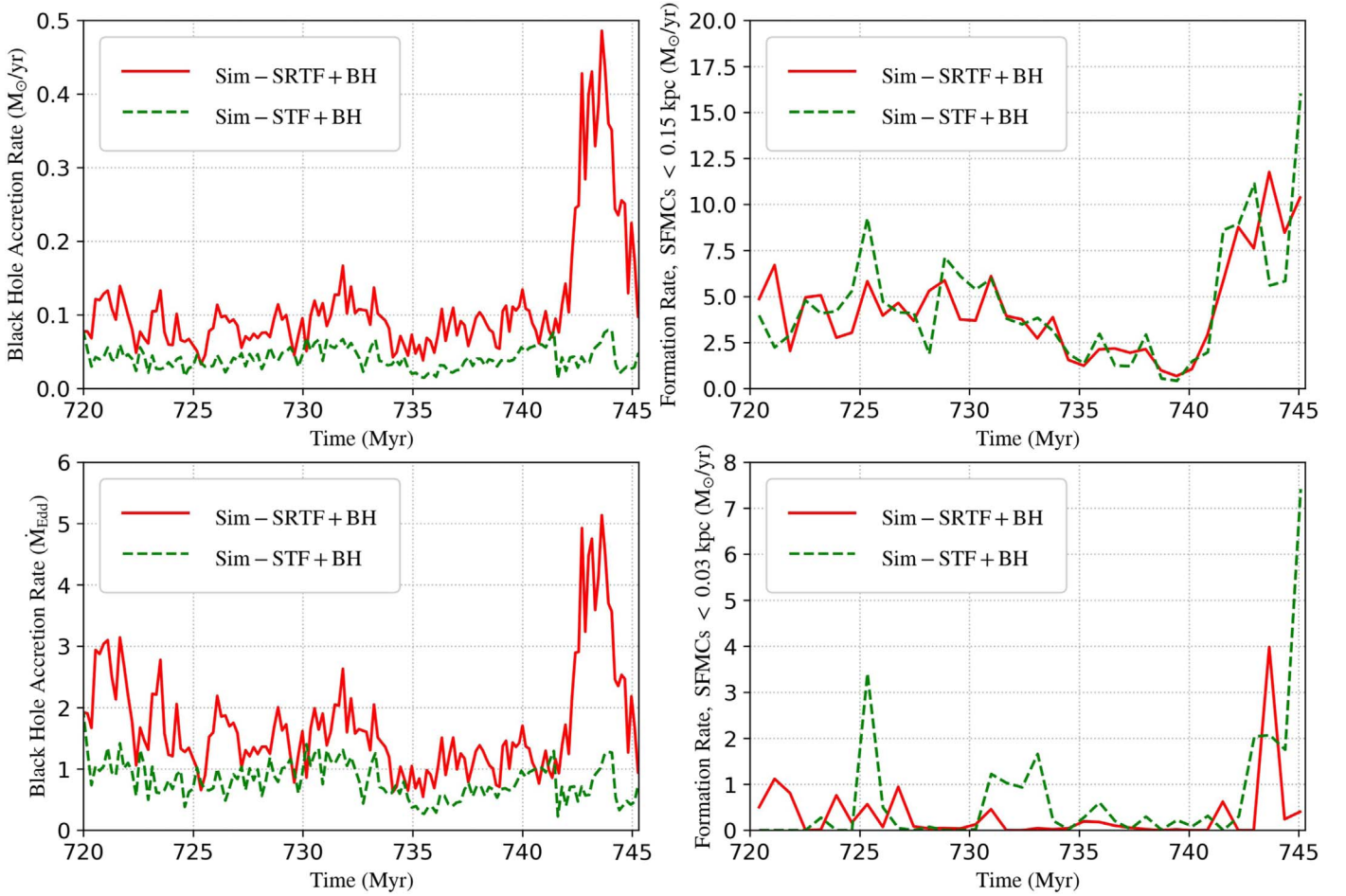


Figure 7. MBH accretion rate in the unit of $M_{\odot} \text{yr}^{-1}$ (top left-hand panel) and M_{Edd} (bottom left-hand panel), and the formation rates of stars (SFMCs) that are located within 150 pc from the MBH at $z = 7.3$ (top right-hand panel) and within 30 pc (bottom right-hand panel). Including the radiation from SFMCs (Sim-SRTF+BH) suppresses star formation in the galactic core region (bottom right-hand panel; see also Figure 6) and helps to retain gas that eventually falls in to the MBH (top left).

the right-hand panel.²² It shows $Q(r) > 1$ at $r \lesssim 100$ pc for Sim-SRTF+BH and Sim-SRTF, implying that the rotating disk in the galactic core is largely stable against fragmentation. This strengthens our notion that the stellar UV radiation, combined with the MBH feedback, helps to retain the gas that could otherwise have been consumed through fragmentation and ensuing star formation. This gas may remain warm on the disk until it eventually accretes on to the MBH. On the other hand, the small sound speed in Sim-STF+BH makes the disk gas marginally unstable with $Q(r) \sim 1$ ($T \sim 10^4$ K in Figure 4), leading to SFMC formation and thus less fuel for the MBH growth.

Our experiments demonstrate that the interplay between gas, stars, and MBHs that was never realized in previous simulations may contain critical information about the expeditious growth of MBHs at high z . Specifically, our results emphasize the need to properly model the *circumnuclear* region in the vicinity of a MBH

²² We modify the Toomre Q parameter on the gaseous disk at radius r as

$$Q(r) = \frac{c_s \Omega(r)}{\pi G (\Sigma_{\text{gas}} + \Sigma_{\text{star}})} \quad (13)$$

where Σ_{gas} and Σ_{star} are the gas and stellar surface density, respectively (Toomre 1964; Wang & Silk 1994). The usual epicycle frequency $\kappa(r) = [rd\Omega^2(r)/dr + 4\Omega^2(r)]^{1/2}$ is replaced by the angular speed $\Omega(r)$ as these two values are in a factor of 2 difference (Wang & Abel 2009).

when performing a high-resolution simulation to probe the growth of a MBH (for more information about interactions between gas, stars, and MBHs in the circumnuclear region of a galaxy, see e.g., Neumayer & Walcher 2012; Antonini 2013; Fiacconi et al. 2013; Wutschik et al. 2013; Naiman et al. 2015; Biernacki & Teyssier 2018). Interested readers may also refer to Section 5.2 for a description of the need for even higher-resolution simulations.

4. Discussion

Before proceeding to conclude the article, we draw the reader's attention to two points that are worthy of brief discussion.

4.1. How to Retain the Fuel to Feed a MBH

The argument in Section 3 that the various modes of SFMC +MBH feedback help to retain the fuel for the MBH growth that could otherwise have been consumed through fragmentation is reminiscent of other numerical studies that have tested rapid black hole growth scenarios. For example, some groups have claimed that the Lyman–Werner background radiation from nearby galaxies could induce halos to collapse isothermally to high densities without fragmenting into smaller clumps. By keeping the gas stable against fragmentation, this mechanism may provide an important pathway to a so-called direct collapse black hole of intermediate size, 10^3 – $10^5 M_{\odot}$

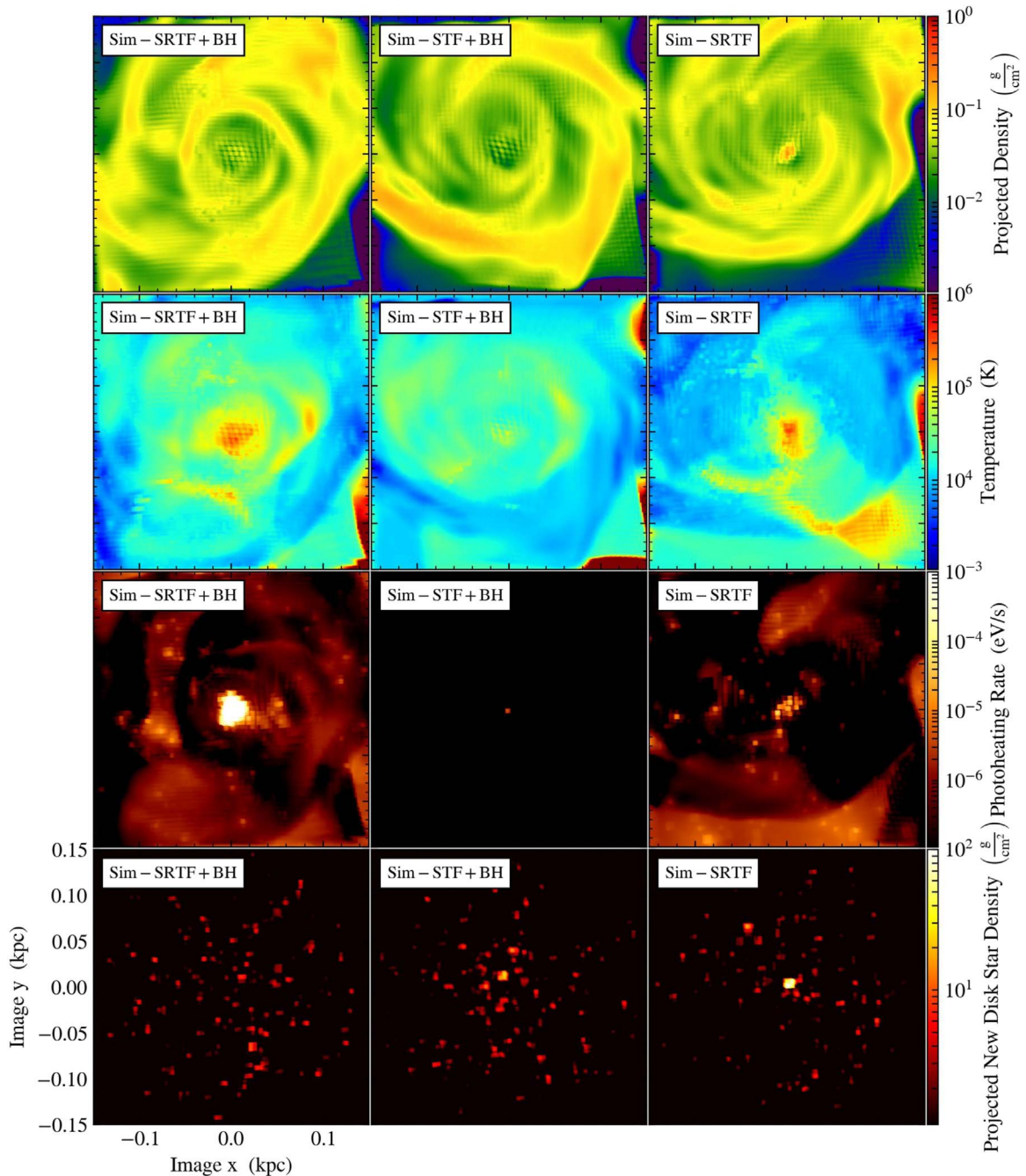


Figure 8. Similar to Figure 3 but in a smaller $(300 \text{ pc})^2$ box centered on the MBH at $z = 7.3$. Shown here are (from top to bottom row) gas surface density, projected temperature (density-weighted), projected photoheating rate (density-weighted), and surface density of “new” disk stars (SFMCs that are within $<30 \text{ pc}$ above and below from the disk plane and are created after $z = 7.5$ when we vary the SFMC/MBH physics in Sections 2.2 and 2.3 between different runs). For more information about the three different simulation runs (from left-hand to right-hand columns), see Table 1 or the caption of Figure 4. The line-of-sight in each panel is parallel to the angular momentum of the inner galactic disk. Radiation from SFMCs and/or the MBH helps to keep hot gas in Sim-SRTF+BH and Sim-SRTF while such heating is negligible in Sim-STF+BH (2nd and 3rd row). In particular, when all of the feedback channels from both SFMCs and the MBH are included, SFMC formation is suppressed in the close vicinity of the MBH (4th row).

(DCBH; e.g., Katz et al. 2015; Regan et al. 2017; Barrow et al. 2018; Wise et al. 2019). Others have asserted that gravoturbulence in multi-scale gas inflows in gas-rich galaxy mergers could prevent fragmentation from occurring, and put the gas Toomre Q parameter above 1 within 30 pc from the galaxy’s center. It thus presents another way to trigger the emergence of DCBH seeds (e.g., Mayer et al. 2015; Mayer & Bonoli 2019). The result of the experiment that we have presented in this paper is broadly in line with these attempts

that are trying to find a viable route to direct gas collapse and expedite the growth of MBHs.

Another mechanism that several numerical studies have recently argued to retain a reservoir of gas to fuel a MBH is through building a compact and massive galactic core (e.g., Dekel et al. 2019, and references therein). The growth of a MBH is slow when the supernova feedback pushes the gas out of the galactic potential well, but once above a critical mass of $M_* \sim 10^{10} M_\odot$ the MBH grows rapidly because the “compaction” near the galaxy

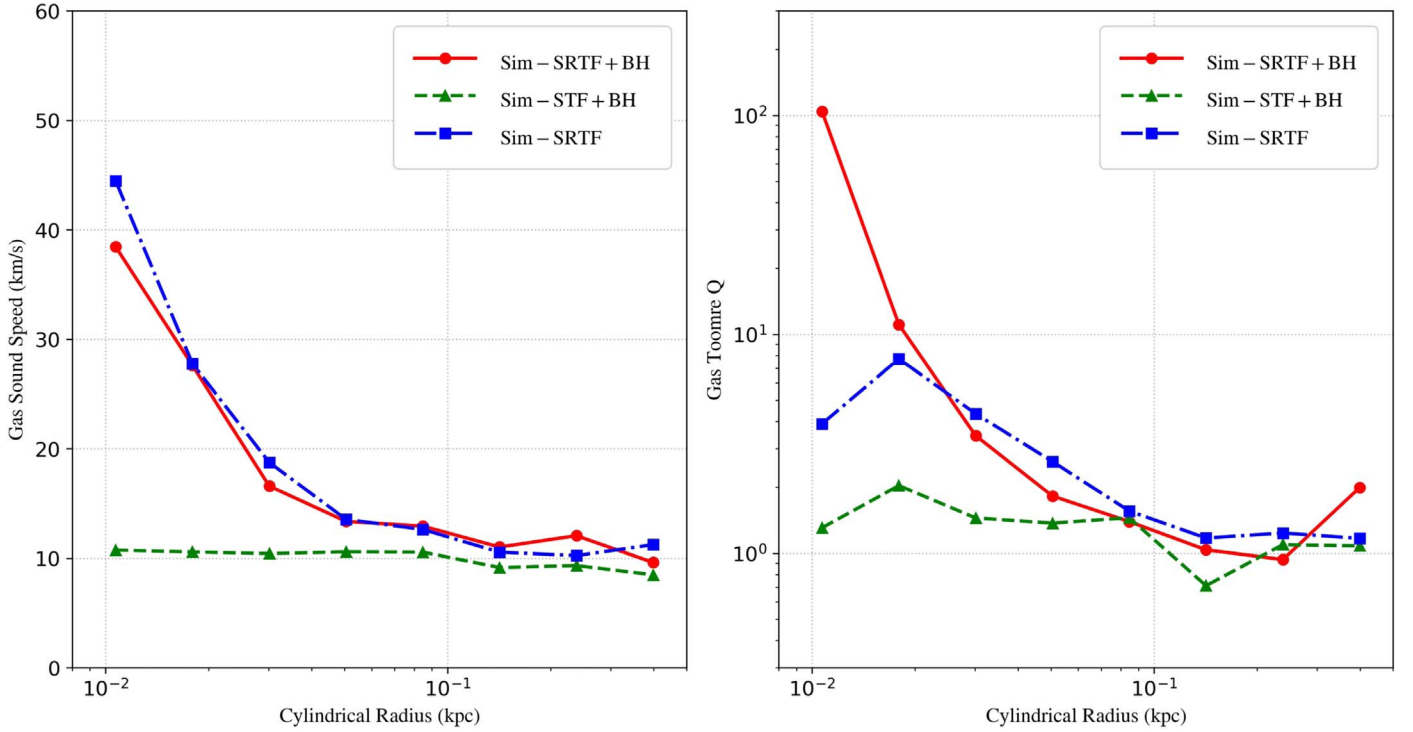


Figure 9. Mass-weighted cylindrical profiles of the sound speed (left-hand panel) and Toomre Q parameter of gas (right-hand panel) in a disk centered on the MBH at $z = 7.3$. The disk has a thickness 60 pc. Due to the radiation mostly by SFMCs, the gas at the galactic core region in Sim-SRTF+BH and Sim-SRTF has large sound speeds (left-hand panel). The gas Toomre Q parameter indicates that the gas within a cylindrical radius of ~ 100 pc from the MBH in Sim-SRTF+BH is mostly stable against fragmentation, while the gas in Sim-STF+BH is marginally unstable (right-hand panel).

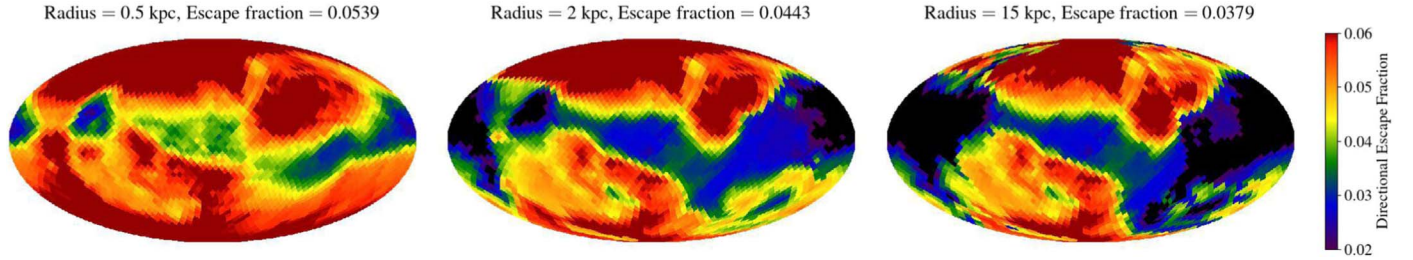


Figure 10. All-sky maps of UV photon escape fractions at 0.5, 2.0 and 15 kpc (from left to right) along different lines of sight from the SFMCs. The equator plane of the map is perpendicular to the angular momentum vector of the galactic disk. The plots are obtained by post-processing the optical depth of hydrogen-ionizing photons in each direction in the Sim-SRTF+BH run at $z = 7.3$. At 15 kpc ($\simeq R_{\text{vir}}$; see Section 2.4), the galactic *average* escape fraction, f_{esc} , is 0.0379 at this epoch. f_{esc} stays around $\lesssim 0.05$ throughout the simulation time. UV photons have harder time to penetrate the thicker neutral hydrogen along the galaxy’s disk plane which is shown here as bluer color (lower escape fraction) along the equator.

center makes the MBH sink to the center and brings the supernova ejecta back to its deep potential (see Figure 8 of Dekel et al. 2019). The target galaxy that we have used in this paper is just around this critical mass with $M_{\text{vir}} \simeq 7 \times 10^{10} M_{\odot}$, $M_{*} \simeq 8 \times 10^9 M_{\odot}$, and the stellar/gas mass within 1 kpc from the center, $M_{*, < 1 \text{ kpc}} \simeq 3 \times 10^9 M_{\odot}$ and $M_{\text{gas}, < 1 \text{ kpc}} \simeq 3 \times 10^8 M_{\odot}$, respectively (see Section 2.4). Indeed, there is a hint that the combination of the compact core (with $\Sigma_{*, < 1 \text{ kpc}} \sim 10^9 M_{\odot} \text{ kpc}^{-2}$) and the SFMC+MBH feedback helps to retain a reservoir of gas to feed the MBH. However, it remains to be seen if this behavior will be sustained beyond the simulation time reported here, ~ 25 Myr.

4.2. Galactic Escape Fraction

Because galaxies are simulated with ionizing photons from SFMCs and MBHs on the fly, we can study how many photons

escape a galaxy using the post-processing machinery developed in Kim et al. (2013a). Interested readers are referred to the Section 5.2 of Kim et al. (2013a) on how an all-sky escape fraction map is built. Figure 10 presents the all-sky maps of escape fraction at various distances along different lines of sight from the SFMCs in Sim-SRTF+BH. As noted on top of each panel, the *average* escape fraction decreases as the column density of neutral hydrogen increases. At 15 kpc ($\simeq R_{\text{vir}}$; Section 2.4), the *average* escape fraction, f_{esc} , is 0.0379 at this epoch, and it stays around $\lesssim 0.05$ throughout the simulation time. UV photons find it more difficult to penetrate the thicker neutral hydrogen along the galaxy’s disk plane, which is shown here as bluer color (lower escape fraction) along the equator.

Although in Figure 3 (4th row) there seems to be an indication that Sim-SRTF+BH has more enhanced UV escape fraction than Sim-SRTF has, we find no such trend in the $\lesssim 20$

snapshots that we stored throughout the simulation time. In other words, Sim-SRTF+BH and Sim-SRTF do not show statistically significant difference in f_{esc} . We suspect that the f_{esc} values of the two runs are similar because the photoionization and clearing of the ISM are done mostly by radiation from SFMCs at these epochs.²³ As seen in Sim-STF+BH (4th row of Figure 3), the MBH’s UV luminosity alone is not enough to carve out pathways for photons to escape. However, the observation that the MBH radiation does not significantly alter f_{esc} should be tested with a run with a longer evolution time (see Section 5.2). Although there may be little AGN contribution to f_{esc} in the particular epoch that we tested, it may become important later (for more discussion on the relative contributions to universe’s reionization by quasars and stellar sources, see, e.g., Robertson et al. 2010; Madau & Haardt 2015).

5. Conclusion

5.1. Summary

Using a state-of-the-art simulation technique on an adaptively refined mesh, a suite of high-resolution simulations of a massive $\sim 7 \times 10^{10} M_{\odot}$ galaxy for ~ 25 Myr at $z \sim 7.5$ has been carried out with a $\gtrsim 10^6 M_{\odot}$ embedded MBH seed, portraying an analog of a fast-growing MBH seed in a high- z galaxy. The high resolution imposed in our simulations allows us to self-consistently incorporate all galactic components and the interactions between them, which are important to understand the high- z quasar-host galaxies. Our simulations feature, most importantly, radiating stars and MBHs because we explicitly trace their photoionizing radiation through a full three-dimensional radiative transfer calculation on the fly. Additional feedback channels, such as supernovae explosions and bipolar winds from a MBH, are also considered (Sections 2.2 and 2.3). To the best of our knowledge, these sophisticated physics models have rarely been realized with sufficient resolution in a galaxy-scale numerical study regarding high- z MBH-host galaxies. In this regard, our approach differs from, and complements, previous studies that have often resorted to thermal or mechanical feedback alone with ad hoc conversion efficiencies, while ignoring the coupling processes of SFMC or MBH feedback with the ISM below resolution.

In this first report, we have focused on the evolution of the MBH seed and the inner region of its host galaxy. We find that feedback from SFMCs and an accreting MBH helps to suppress star formation locally in the galactic core region (Section 3.1). Newly included radiation feedback from SFMCs, combined with feedback from the MBH, prevents

²³ The total UV luminosity of “new” SFMCs in our calculation is

$$\begin{aligned} L_{\text{MC}}(t) &= q_{\text{MC}} E_{\text{ph}} \dot{M}_{\text{MC}}(t) \\ &\sim 6.3 \times 10^{46} \times 16.0 \times \dot{M}_{\text{MC}}(t) \text{ eV s}^{-1} \\ &\sim 10^{44} \text{ erg s}^{-1} [\dot{M}_{\text{MC}}(t)/10^8 M_{\odot}], \end{aligned} \quad (14)$$

from Equation (4) and Figure 6, whereas the total UV luminosity of a $\sim 2 \times 10^6 M_{\odot}$ MBH accreting at the Eddington rate is

$$\begin{aligned} L_{\text{BH,UV}}(t) &= 0.5 f_{\text{UV}} \epsilon_r \dot{M}_{\text{BH}}(t) c^2 \\ &\sim 0.5 \times 0.1 \times 0.1 \times \dot{M}_{\text{BH}}(t) \times c^2 \\ &\sim 10^{43} \text{ erg s}^{-1} [\dot{M}_{\text{BH}}(t)/0.05 M_{\odot} \text{ yr}^{-1}], \end{aligned} \quad (15)$$

from Equation (10). This suggests that for our young, fast-growing target galaxy at $z = 7.5$, the UV radiation could be dominated by SFMCs.

runaway star formation from occurring and helps to retain gas that eventually accretes on to the MBH. This results in an increased growth rate of the MBH when compared with the run without stellar radiation feedback (Section 3.2). Because this was the first time that the radiative feedback channels of stars and MBHs have been used together in a galaxy-scale simulation, we are able to demonstrate that previously undiscussed types of interplay between gas, SFMCs, and a MBH may hold important clues about the growth and feedback of quasars and their host galaxies at high z . We argue that this finding is broadly in line with the previous studies, which attempts to not only find a route to avoid fragmentation of interstellar gas but also to contribute more directly to rapid MBH growth (Section 4.1).

The comprehensive numerical framework that we have developed for the present study is able to overcome the “mismatch” between the cutting-edge resolution in the field and the physics models used in simulations. Our tests verify that the simulations that adopt the proposed numerical framework are computationally feasible on commercially available cluster architectures with sufficiently large memories. This opens up many potential applications of our numerical framework—including, but not simply limited to, a deeper look into the high- z quasar-host galaxies with even higher resolution. The future directions of this line of work are discussed in the next subsection.

5.2. Future Work

Because we strive to calculate the impact of stellar and MBH feedback energy in the ISM from first principles—rather than tuning it to match observed galaxies—and explore previously undiscussed interplay between galactic ingredients, our simulation technique can offer a unique perspective for the growth of high- z MBHs and their hosts. Obviously, the present study suffers from various limitations, which we will list below. We are actively testing and running next generation simulations to expand the scope of our research.

1. Currently, the simulation barely resolves the scale of star-forming gas clumps and the gas flows at the Bondi radius near a MBH (see Section 2.3; $\Delta x_{14} = 4.79$ pc at $z = 7.5$). This was done by employing a strategy to re-simulate an interesting time interval with increased resolution (Section 2.4). A similar technique could be used recursively to further increase resolution between multi-scale re-runs. Our simulation will be able to follow the actual gas inflows from galaxy- to sub-pc scale in a violent merging event for which the gas distribution can rarely be idealized as an exponential form—as is sometimes assumed in previous studies, such as Hopkins & Quataert (2010).²⁴ This type of simulation could help us evaluate how galaxy mergers and the triggered MBH activities affect the buildup of high- z quasars, and/or initiate a quasar-regulated star formation phase.
2. Due to computational limitations, the reported run time is ~ 25 Myr at around $z \sim 7.5$ (for “Sim-SRTF+BH”). As

²⁴ Note that our re-simulation technique improves that of Hopkins & Quataert (2010), which is one of the most successful attempts to render gas inflows from kpc to sub-pc scale. However, to setup a gas distribution for a high-resolution re-simulation, they used an idealized, exponential gas disk motivated by the lower-resolution run. In contrast, we plan to adopt the exact gas distribution from the lower-resolution run but with increased resolution.

we advance our simulation for a longer evolution time with better optimizations, we expect to acquire more complete understandings of nonlinear interactions between galactic ingredients occurring at widely different scales simultaneously—from sub-pc scale to $\gtrsim R_{\text{vir}}$ scale. For example, we could be poised to study the effect of MBH-driven outflows on gas cooling in the disk and gaseous halo, and also if this could alter the star formation history by suppressing cooling and/or gas inflows for a sufficiently long time.

3. By building a suite of cosmological “zoom-in” simulations, we aim to validate the proposed pathways to extremely massive quasars at $z > 7$. This type of experiment will significantly advance our understanding of the neighborhood of MBHs (such as accretion disk and nuclear disk), and predict their characteristics. While challenging, this is a well-timed study because these observations provide excellent constraints on the growths of high- z galaxies and MBHs (Section 1). More sophisticated physics for MBHs—which are absent in the present runs but appropriate at the adopted resolution scale—should be taken into consideration to refine our estimates—such as an MBH accretion model considering angular momentum (not the plain Bondi estimate, Equation (7)), panchromatic radiation from a MBH (as opposed to monochromatic one), and outflows from a MBH interacting with magnetic fields (Butsky et al. 2017).

The authors thank Heon-Young Chang, Mark Krumholz, Myeong-Gu Park, and Hao-Yi Wu for insightful discussions during the progress of this study. We also thank the anonymous referee who helped significantly improve the draft of this paper. J.K. acknowledges support by Samsung Science and Technology Foundation under Project Number SSTF-BA1802-04, and by Research Start-up Fund for the new faculty of Seoul National University. J.W. is supported by National Science Foundation grants AST-1614333 and OAC-1835213 and NASA grant NNX17AG23G. The computing time used for the presented simulation was in part provided by Extreme Science and Engineering Discovery Environment (XSEDE) allocations TG-AST140023 and TG-AST140064. XSEDE is supported by the National Science Foundation (NSF) grant ACI-1053575. Resources supporting this work were also provided by the NASA High-End Computing (HEC) Program through the NASA Advanced Supercomputing (NAS) Division at Ames Research Center. This work was also supported by the National Institute of Supercomputing and Network/Korea Institute of Science and Technology Information with supercomputing resources including technical support, grants KSC-2018-S1-0016 and KSC-2018-CRE-0052. The publicly available ENZO and yt codes that we have used in this work are the products of collaborative efforts by many independent scientists from numerous institutions around the world. Their commitment to open science has helped to make this work possible.

ORCID iDs

Ji-hoon Kim  <https://orcid.org/0000-0003-4464-1160>
 John H. Wise  <https://orcid.org/0000-0003-1173-8847>
 Joel R. Primack  <https://orcid.org/0000-0001-5091-5098>
 Philip F. Hopkins  <https://orcid.org/0000-0003-3729-1684>

References

- Abel, T., & Wandelt, B. D. 2002, *MNRAS*, **330**, L53
 Anninos, P., Zhang, Y., Abel, T., & Norman, M. L. 1997, *NewA*, **2**, 209
 Antonini, F. 2013, *ApJ*, **763**, 62
 Aykutalp, A., Wise, J. H., Spaans, M., & Meijerink, R. 2014, *ApJ*, **797**, 139
 Bañados, E., Venemans, B. P., Mazzucchelli, C., et al. 2018, *Natur*, **553**, 473
 Barrow, K. S. S., Aykutalp, A., & Wise, J. H. 2018, *NatAs*, **2**, 987
 Bieri, R., Dubois, Y., Rosdahl, J., et al. 2017, *MNRAS*, **464**, 1854
 Biernacki, P., & Teyssier, R. 2018, *MNRAS*, **475**, 5688
 Bondi, H. 1952, *MNRAS*, **112**, 195
 Bryan, G. L., & Norman, M. L. 1997, in ASP Conf. Ser. 123, Computational Astrophysics; 12th Kingston Meeting on Theoretical Astrophysics, ed. D. A. Clarke & M. J. West (San Francisco, CA: ASP), 363
 Bryan, G. L., Norman, M. L., O’Shea, B. W., et al. 2014, *ApJS*, **211**, 19
 Butsky, I., Zrake, J., Kim, J.-h., Yang, H.-I., & Abel, T. 2017, *ApJ*, **843**, 113
 Ceverino, D., Klessen, R. S., & Glover, S. C. O. 2018, *MNRAS*, **480**, 4842
 Ceverino, D., & Klypin, A. 2009, *ApJ*, **695**, 292
 Ciotti, L., Ostriker, J. P., & Proga, D. 2009, *ApJ*, **699**, 89
 Costa, T., Rosdahl, J., Sijacki, D., & Haehnelt, M. G. 2018, *MNRAS*, **473**, 4197
 Debuhr, J., Quataert, E., & Ma, C.-P. 2011, *MNRAS*, **412**, 1341
 DeGraf, C., & Sijacki, D. 2017, *MNRAS*, **466**, 3331
 Dekel, A., Lapiner, S., & Dubois, Y. 2019, arXiv:1904.08431
 Fiacconi, D., Madau, P., Potter, D., & Stadel, J. 2018, *ApJ*, **824**, 144
 Fiacconi, D., Mayer, L., Roškar, R., & Colpi, M. 2013, *ApJL*, **777**, L14
 Hahn, O., & Abel, T. 2011, *MNRAS*, **415**, 2101
 Haiman, Z., & Loeb, A. 2001, *ApJ*, **552**, 459
 Hopkins, P. F., Kereš, D., Oñorbe, J., et al. 2014, *MNRAS*, **445**, 581
 Hopkins, P. F., & Quataert, E. 2010, *MNRAS*, **407**, 1529
 Hopkins, P. F., Wetzell, A., Kereš, D., et al. 2018, *MNRAS*, **480**, 800
 Katz, H., Sijacki, D., & Haehnelt, M. G. 2015, *MNRAS*, **451**, 2352
 Kim, J.-h. 2011, PhD Dissertation, Stanford Univ.
 Kim, J.-h., Abel, T., Agertz, O., et al. 2014, *ApJS*, **210**, 14
 Kim, J.-h., Agertz, O., Teyssier, R., et al. 2016, *ApJ*, **833**, 202
 Kim, J.-h., Krumholz, M. R., Wise, J. H., et al. 2013a, *ApJ*, **775**, 109
 Kim, J.-h., Krumholz, M. R., Wise, J. H., et al. 2013b, *ApJ*, **779**, 8
 Kim, J.-h., Ma, X., Grudić, M. Y., et al. 2018, *MNRAS*, **474**, 4232
 Kim, J.-h., Wise, J. H., Alvarez, M. A., & Abel, T. 2011, *ApJ*, **738**, 54
 Komatsu, E., Smith, K. M., Dunkley, J., et al. 2011, *ApJS*, **192**, 18
 Koyama, H., & Inutsuka, S. 2002, *ApJL*, **564**, L97
 Krumholz, M. R., & Tan, J. C. 2007, *ApJ*, **654**, 304
 Krumholz, M. R., & Thompson, T. A. 2013, *MNRAS*, **434**, 2329
 Latif, M. A., Volonteri, M., & Wise, J. H. 2018, *MNRAS*, **476**, 5016
 Lupi, A., Haardt, F., Dotti, M., et al. 2016, *MNRAS*, **456**, 2993
 Madau, P., & Haardt, F. 2015, *ApJL*, **813**, L8
 Mayer, L., & Bonoli, S. 2019, *RPPH*, **82**, 016901
 Mayer, L., Fiacconi, D., Bonoli, S., et al. 2015, *ApJ*, **810**, 51
 Mortlock, D. J., Warren, S. J., Venemans, B. P., et al. 2011, *Natur*, **474**, 616
 Murray, N., Quataert, E., & Thompson, T. A. 2010, *ApJ*, **709**, 191
 Murray, N., & Rahman, M. 2010, *ApJ*, **709**, 424
 Naiman, J. P., Ramirez-Ruiz, E., Debuhr, J., & Ma, C.-P. 2015, *ApJ*, **803**, 81
 Neumayer, N., & Walcher, C. J. 2012, *AdAst*, **2012**, 709038
 Norman, M. L., & Bryan, G. L. 1999, *ASSL*, **240**, 19
 Norman, M. L., Bryan, G. L., Harkness, R., et al. 2007, arXiv:0705.1556
 Regan, J. A., Downes, T. P., Volonteri, M., et al. 2019, *MNRAS*, **486**, 3892
 Regan, J. A., Visbal, E., Wise, J. H., et al. 2017, *NatAs*, **1**, 0075
 Robertson, B. E., Ellis, R. S., Dunlop, J. S., McLure, R. J., & Stark, D. P. 2010, *Natur*, **468**, 49
 Salpeter, E. E. 1955, *ApJ*, **121**, 161
 Sazonov, S. Y., Ostriker, J. P., & Sunyaev, R. A. 2004, *MNRAS*, **347**, 144
 Shakura, N. I., & Sunyaev, R. A. 1973, *A&A*, **24**, 337
 Sijacki, D., Vogelsberger, M., Genel, S., et al. 2015, *MNRAS*, **452**, 575
 Smidt, J., Whalen, D. J., Johnson, J. L., Surace, M., & Li, H. 2018, *ApJ*, **865**, 126
 Stinson, G. S., Brook, C., Macciò, A. V., et al. 2013, *MNRAS*, **428**, 129
 Stone, J. M., & Norman, M. L. 1992a, *ApJS*, **80**, 753
 Stone, J. M., & Norman, M. L. 1992b, *ApJS*, **80**, 791
 Sutherland, R. S., & Dopita, M. A. 1993, *ApJS*, **88**, 253
 Toomre, A. 1964, *ApJ*, **139**, 1217
 Trebitsch, M., Volonteri, M., Dubois, Y., & Madau, P. 2018, *MNRAS*, **478**, 5607
 Turk, M. J., Smith, B. D., Oishi, J. S., et al. 2011, *ApJS*, **192**, 9
 Vázquez-Semadeni, E., Colín, P., Gómez, G. C., Ballesteros-Paredes, J., & Watson, A. W. 2010, *ApJ*, **715**, 1302
 Venemans, B. P., Findlay, J. R., Sutherland, W. J., et al. 2013, *ApJ*, **779**, 24

- Volonteri, M. 2010, [A&ARv](#), **18**, 279
- Wang, B., & Silk, J. 1994, [ApJ](#), **427**, 759
- Wang, P., & Abel, T. 2009, [ApJ](#), **696**, 96
- Wang, P., Li, Z., Abel, T., & Nakamura, F. 2010, [ApJ](#), **709**, 27
- Weinberger, R., Springel, V., Hernquist, L., et al. 2017, [MNRAS](#), **465**, 3291
- Whalen, D., & Norman, M. L. 2006, [ApJS](#), **162**, 281
- Wise, J. H., & Abel, T. 2011, [MNRAS](#), **414**, 3458
- Wise, J. H., Regan, J. A., O'Shea, B. W., et al. 2019, [Natur](#), **566**, 85
- Wu, X.-B., Wang, F., Fan, X., et al. 2015, [Natur](#), **518**, 512
- Wutschik, S., Schleicher, D. R. G., & Palmer, T. S. 2013, [A&A](#), **560**, A34